Journal of Drug Delivery Science and Technology 120 (2026) 108250

Contents lists available at ScienceDirect

Journal of Drug Delivery Science and Technology

journal homepage: www.elsevier.com/locate/jddst

Novel nano-electrospuns with superparamagnetic and NIR photo-responsive behaviors as smart drug delivery systems and biomedical applications

Sergio Sciré [a], Achraf Derbel [b], Francesca Terracina [a], Emanuela Fabiola Craparo [a], Luca Cicero [c], Giovanni Cassata [c], Carlo Trigona [b], Mariano Licciardi [a,*]

[a] Department of Biological, Chemical and Pharmaceutical Sciences and Technologies (STeBiCeF), University of Palermo, Via Archirafi 30, Palermo, 90123, Italy
[b] Department of Electrical Electronic and Computer Engineering, University of Catania, Viale Andrea Doria 6, Catania, 95125, Italy
[c] Centro Mediterraneo Ricerca e Training (Ce.Me.Ri.T), Istituto Zooprofilattico Sperimentale della Sicilia "A. Mirri", Via Gino Marinuzzi 3, Palermo, 90129, Italy

ARTICLE INFO

Keywords:
Poly(butylene succinate)
Photo-thermal effect
Iron oxide nanoparticles
Ciprofloxacin
External stimuli responsive
Electrospinning
Superparamagnetic
NIR responsive material electrospun scaffolds
Controlled drug release
MRI-Visible materials

ABSTRACT

Smart Drug Delivery Systems (SDDSs) are advanced platforms enabling controlled and stimuli-responsive drug release. Among external stimuli, near-infrared (NIR) light and magnetic fields are particularly attractive due to their non-invasive activation and tunable energy conversion. Multifunctional electrospun scaffolds (PCI) based on poly(butylene succinate) (PBS), ciprofloxacin (CPX), and iron oxide nanopowder (INPs, d < 50 nm) as a low-cost superparamagnetic component has been exhaustively explored, reporting the use of INP as photothermal agent in electrospun scaffolds, enabling high nanoparticle loading and NIR-triggered drug release, a strategy still scarcely explored in electrospun systems. This powder-based strategy simplifies formulation compared to stabilized SPION dispersions while preserving magnetic and photothermal functionalities. The resulting mats exhibited uniform, defect-free fibers with tunable mechanical properties and sustained CPX release (≈40% over 11 days), which increased to ≈60% under NIR irradiation. INPs imparted superparamagnetic behavior, NIR responsiveness, and MRI and X-ray detectability, while CPX improved fiber morphology and surface wettability. High cell viability (>85%) confirmed the cytocompatibility of the scaffolds. Comprehensive characterization included morphology, wettability, thermal and mechanical properties, NIR response, and drug release. Magnetic properties were evaluated using a cost-effective sensor-based approach (Hall sensors and fluxgate magnetometer), confirming superparamagnetic behavior. By coupling NIR-triggered drug release with MRI detectability, PCI scaffolds provide a compact theranostic platform for localized biomedical applications. Overall, PCI scaffolds represent a scalable and cost-effective multifunctional platform integrating controlled drug delivery, photothermal responsiveness, and imaging capability, showing strong potential for advanced biomedical applications.

1. Introduction

Smart Drug Delivery Systems (SDDSs) represent a major advancement in pharmaceutical technology and nanomedicine, enabling controlled, targeted, and stimuli-responsive drug release [1]. These systems can respond to physiological or pathological stimuli, such as pH, temperature, or specific biomarkers, as well as to external triggers including electromagnetic radiation, magnetic fields, or light, allowing localized and tunable therapeutic activation [2–5]. Among external stimuli, near-infrared (NIR) irradiation is particularly attractive due to its deep tissue penetration and minimal phototoxicity [6–9]. NIR-responsive systems can induce localized heating, enabling photothermal therapy and controlled drug release through photothermal agents such as iron oxide nanoparticles, gold nanostructures, carbon-dots, MOFs and COFs, or hybrid materials [10–25]. Photo-thermal electrospinning (PTE) has recently emerged as a promising approach to integrate electrospun fibrous scaffolds with photothermal functionality [26]. This strategy combines the advantages of electrospinning, such as high surface area, tunable mechanical properties, and extracellular matrix mimicry, with externally triggered therapeutic activation [27–29]. However, the development of simple, scalable, and efficient NIR-responsive electrospun systems remains limited [30].

* Corresponding author.
E-mail address: mariano.licciardi@unipa.it (M. Licciardi).

https://doi.org/10.1016/j.jddst.2026.108250
Received 1 December 2025; Received in revised form 5 March 2026; Accepted 16 March 2026
Available online 17 March 2026

Superparamagnetic iron oxide nanoparticles (SPIONs) exhibit unique physicochemical and magnetic properties that make them highly suitable for biomedical applications and theranostics [31–33]. They have been widely investigated for cancer therapy, imaging, and magnetically triggered drug delivery [11,34–37], are characterized by high biocompatibility and potential biodegradability [38,39]. In addition, NIR-mediated photothermal heating can enhance magnetic hyperthermia effects [40–42], while the NIR window offers advantages such as low tissue absorption, and compatibility with clinical technologies [43]. However, a critical limitation of conventional SPION-based electrospun nanofiber scaffolds lies in their typical availability as stabilized dispersions [44], which are often incompatible with electrospinning solvent systems and may increase formulation complexity and cost. In contrast, dry iron oxide nanopowder (INP) represents a simple, scalable and cost-effective alternative, overcoming solvent compatibility issues and enabling higher nanoparticle loading. To the best of our knowledge, this is the first study reporting the use of dry INPs as photothermal agents in electrospun scaffolds, enabling both superparamagnetic behavior and NIR-triggered drug release, a strategy still scarcely explored in electrospun systems. This approach differs from conventional SPION-based systems, which typically rely on stabilized dispersions and more complex processing strategies. In this work, multifunctional photothermal electrospun scaffolds (PCI) based on Poly(butylene succinate) (PBS), ciprofloxacin (CPX), and iron oxide nanopowder (INPs) were developed. PBS has proven to be a promising polymer for electrospun applications, owing to its biodegradability, biocompatibility, and tunable physicochemical properties [45–53]. Although the present study does not specifically employ green nanomaterials, PBS can be produced from renewable resources via biotechnological routes, supporting a more sustainable material design [54]. CPX was selected for its antibacterial activity and its ability to improve fiber morphology [55], while INPs impart magnetic responsiveness, NIR-induced photothermal behavior, and imaging capability. Compared to conventional photothermal nanoparticle systems, electrospun fiber-based patches enable localized retention and reduced systemic exposure [56]. To systematically investigate the influence of formulation parameters, CPX and INP concentrations were varied based on evidence and processability constraints, ensuring optimal fiber formation, homogeneous component distribution, and effective stimuli responsive behavior. The resulting scaffolds were extensively characterized in terms of morphology, physicochemical properties, drug release, NIR responsiveness, biocompatibility, and magnetic behavior, evaluated using cost-effective sensor-based approaches [57,58]. Overall, the proposed PCI scaffolds represent a scalable and cost-effective multifunctional platform integrating controlled drug delivery, NIR-triggered photothermal responsiveness, and magnetic detectability. The use of dry iron oxide nanopowder as a dual photothermal and magnetic agent, combined with its implementation within electrospun systems, highlights a still underexplored yet highly promising strategy for the development of advanced theranostic biomaterials.

2. Materials and methods

2.1. Materials

1,1,1,3,3,3-Hexafluoropropan-2-ol (HFIP) was purchased from Fluorochem, Hadfield GB, Poly(1,4-butylene succinate) extended with 1,6-diisocyanatohexane (PBS), Ciprofloxacin (CPX), Iron nano-powder (INP, Fe_3O_4) with a diameter <50 nm, dichloromethane (99.9%, DCM), hydrochloric acid (37%), phenanthroline, hydroxylamine hydrochloride, sodium acetate, glacial acetic acid, Dulbecco Modified Eagle's Medium (DMEM), fetal bovine serum (FBS), glutamine, penicillin (100 U ml^{-1}), streptomycin (100 μg mL^{-1}), amphotericin B, and Alamar Blue (AB) assay kit were purchased from Sigma Aldrich Merck, Milan Italy, and used as received. Human gingival fibroblasts (HGF-1) and human epidermal keratinocytes (HA-CAT) cells were provided from Istituto zooprofilattico sperimentale della Lombardia e dell'Emilia Romagna.

2.2. Methods

2.2.1. Electrospinning of the magnetic nano-electrospuns

Three scaffolds with different contents of ciprofloxacin (CPX) and iron nanopowder having diameter <50 nm (INP) were electrospinned; 750 mg of Poly(1,4-butylene succinate) extended with 1,6-diisocyanatohexane (PBS) were dissolved in 1,1,1,3,3,3-Hexafluoropropan-2-ol (HFIP) (5 ml) by gentle stirring. Then 41.7 mg of CPX and after solubilization 41.7 mg of INP were added to produce PCI having 5% of both CPX and INP; 44.5 mg of CPX and 89 mg of INP were added to produce PCI having 5% of CPX and 10% of INP respectively; or 215 mg of CPX and 107.5 of INP were added to have a PCI with 20% of CPX and 10% of INP. The obtained suspensions were stirred and sonicated cyclically for 3 h at intervals of 30 min, then left under stirring overnight at room temperature (visual assessment of dispersion stability is provided in the photos of Figs. S1 and S2 of Supplementary Materials). The electrospinning was always performed the day after using the MECC NF 104 electrospinning prototyping system. The solution was sprayed using a 5 ml Terumo syringe fitted with a 20-gauge needle. A rotating cylinder, 4 cm in diameter, was used as collector. The electrospun scaffolds were carefully cut longitudinally, unfolded, and gently taken out from the collector to form a mat measuring approximatively 12 × 4 cm (see Fig. S3 of Supplementary Materials). The spinning parameters used for the whole spinning process were: feed rate 0.8 mL/h, voltage 15 kV, volume 5 mL, needle to collector distance 10 cm, collector rotation speed 250 rpm, traverse speed 20 mm/s, traverse distance 120 mm. Ambient temperature during electrospinning was 23–25 °C, and relative humidity was approximately 50%. These conditions were not strictly controlled but were recorded as set by the centralized heating and conditioning system.

2.2.2. Scanning Electron Microscopy (SEM) of the magnetic nano-electrospuns

SEM analyses were conducted to investigate the microscopic morphology of PBS scaffolds. The measurements were conducted by a Phenom Pro X (AlfaTest) operating at 10 kV and at different magnifications (4000×, 9000x and 16500x) to highlight progressively microstructural details. The samples, when necessary, were sputtered with 10 nm gold nanoparticles, before performing acquisitions. Properly acquired not gold covered SEM images with high contrast were processed using ImageJ software to determine the average dimensional distribution of fibers, based on the measurement of 122 individual fibers. Results were expressed as mean ± standard deviation (SD), providing quantitative insights into the morphological variations across different sample types. During SEM analysis with not treated, energy-dispersive X-ray spectroscopy (EDX) was also performed to obtain information on the chemical elements present on the surface of the scaffolds.

2.2.3. Micro-CT of the magnetic nano-electrospuns

The micro-Computed Tomography (micro-CT) analysis was performed using a Skyscan 1272, Bruker Kontich, Belgium micro-CT scanner. By putting down a coating of wax, one side of the sample was kept fixed on the spinning support of the instrument. The images were acquired by setting a rotation step of 0.2° with a pixel size of 0.3 μm. An X-ray beam with a source voltage of 40 kV and a source current of 250 mA was used. 'Oversize' and 'Batch Scanning' functions were used to visualize the entire sample in high-resolution mode.

2.2.4. Resonance Magnetic Images (RMI) of the magnetic nano-electrospuns

Magnetic resonance imaging was performed using a PharmaScan 70/16 US scanner operating at 7 T (Bruker, Ettlingen, Germany), equipped with a 23 mm volume transmit/receive coil. Axial images were acquired using a scaffold with a thickness of 0.37 mm. The field of view (FOV) was

set to 20 mm × 20 mm, with an in-plane resolution of 256 μm × 256 μm.

2.2.5. Drug and iron loading of the magnetic nano-electrospuns

Theoretical drug loading (DL_T) and iron loading (IL_T), defined respectively as the amount of ciprofloxacin and iron oxide incorporated into the dispersion prior to electrospinning, were calculated as the percentage of the weight of each component relative to the total weight of all constituents used in scaffold preparation, according to the following equations:

$$DL_T\% = \frac{mgCPX}{mgINP + mgCPX + mgPBS} \text{ x100} \quad (1)$$

$$IL_T\% = \frac{mgINP}{mgINP + mgCPX + mgPBS} \text{ x100} \quad (2)$$

The actual amount of ciprofloxacin (CPX) loaded into the nanofibrous scaffolds was quantified by dissolving the patches in chloroform, filtering the solution through a PTFE syringe filter, and analyzing it spectrophotometrically using a Jasco V760 UV–Vis spectrophotometer. Absorbance was measured at the maximum wavelength (λ_{max}) of 284 nm, using a 1 mL quartz cuvette with a 10 mm optical path. Quantification was performed using a calibration curve constructed from UV spectra of CPX standard solutions at known concentrations in dichloromethane (Fig. S1a).

The actual iron content in the scaffolds was determined by colorimetric analyses using an adaptation of the standard "3500-Fe B. Phenanthroline method" of National Environment Methods Index (NEMI) of U.S. government, for iron determination. Briefly a precisely weighed sample (about 10 mg) was brought into contact with 6N hydrochloric acid. After complete digestion and dissolution, the solution was evaporated to dryness. The residue was reconstituted with 10 μL of 6 N HCl and 990 μL of distilled water to ensure rapid and complete dissolution. Then, 9 mL of acetate buffer (pH 5.5) were added. An aliquot of 700 μL of the reconstituted solution was mixed with 100 μL of a 10% aqueous hydroxylamine solution and 200 μL of a 2% 1,10-phenanthroline solution. After 30 min of reaction, absorbance measurements were performed in triplicate using an Eppendorf AF2200 plate reader at a wavelength of 540 nm, in a 96-well plate. Quantification was based on a calibration curve prepared from the same iron powder used for electrospinning (seven points, concentrations ranging from 7 μg/mL to 37 μg/mL) (Fig. S1b), treated under the same conditions as the samples. Results were calculated and expressed as INP content.

2.2.6. Attenuated total reflection Fourier transform infrared spectroscopy (FTIR-ATR) analysis of the magnetic nano-electrospuns

FTIR-ATR analyses of the scaffolds and the starting materials were performed using an FTIR spectrometer equipped with an ATR (Bruker, ALPHA, platinum-ATR), recording spectra within a range of 500 to 4000 cm^{-1} (16 scans, resolution of 4 cm^{-1}).

2.2.7. Contact angle measurements of the magnetic nano-electrospuns

Contact angle measurements were performed at ambient temperature and humidity on biomaterial discs with a diameter of 8 mm. Water droplets (volume = 0.02 ml) were deposited on the surface and observed for approximately 1 min. Side profiles of the droplets were captured every 5 s and subsequently analyzed. Measurements were conducted on four separate samples. The results were confronted with patches made of only PBS.

2.2.8. Water up-take of the magnetic nano-electrospuns

These tests consisted of water uptake studies involving PCI patches loaded, and control pure PBS patches. Precisely weighed biomaterial discs were placed in vials filled with phosphate-buffered saline (PBS, pH 7.4) and in vials filled with acetate buffer (pH 5.5), and the weights after 1 h, 2 h, 4 h, and 24 h were measured. All the studies were done in triplicate for PCI and PBS patches, and the data are presented as the average ± standard deviation. The patches at the previously set times were gently blotted on filter papers and then weighed out. The data are presented as the relative percentage increase in weight over time based on the initial dry patch weight.

2.2.9. Determination of the degradation kinetics of the magnetic nano-electrospuns

The degradation rate of the composite PCI was evaluated by measuring the weight loss of samples in PBS at pH 7.4 and Acetate Buffer at pH 5.5 at 37 °C. Samples were immersed in the medium and maintained in an orbital shaker (100 rpm) for four months. At established time intervals (1,2,3,4,5 months), three samples were rinsed thoroughly with water, dried, and weighed again. The percentage weight loss ($W_l(\%)$) was calculated using the equation:

$$W_l(\%) = \frac{W_0 - W_f}{W_0} \cdot 100 \quad (3)$$

where W_0 is the initial dry weight of the disc, and W_f is the final dry weight of the disc.

2.2.10. Water vapor transmission rate (WVTR) of the magnetic nano-electrospuns

The scaffolds' water vapor transmission rate (WVTR) was assessed following the ASTM (American Society for Testing and Materials) standard, under conditions of 25 °C and 38 °C and 90 % relative humidity, using distilled water, by a Permeh$_2$O ExtraSolution instrument. The analysis was performed in triplicate and results were expressed as mean permeability ($g/m^2 \cdot 24$ h) ± standard deviation (mean ± SD, n = 3).

2.2.11. Heating studies under NIR irradiation of the magnetic nano-electrospuns

Heating experiments under near-infrared (NIR) irradiation were performed to evaluate the photothermal response of magnetic nanoelectrospun patches under both high- and low-irradiance conditions. Circular samples of different sizes were used depending on the experimental setup.

For high-irradiance experiments, a circular patch (diameter 5 mm, area ≈0.196 cm^2) was fixed at the bottom of a glass Petri dish (diameter 5.5 cm) and immersed in 1 cm of phosphate-buffered saline (PBS, pH 7.4) under magnetic stirring. The NIR source was positioned 5 cm above the solution surface. Irradiation was carried out at power levels of 5 and 10 W, using a beam radius matching that of the sample, corresponding to power densities of 25.5 and 51.02 W/cm^2, respectively. Temperature changes were monitored using a thermometric probe placed 2.5 cm from the patch. Patches PCI5-5, PCI5-10, and PCI20-10 were tested. For low-irradiance experiments, circular scaffolds (diameter 1 cm) were placed in a plastic Petri dish (diameter 3.5 cm) containing 2 mL of PBS (pH 7.4). Irradiation was performed at a fixed power of 1 W, varying the beam spot size to obtain irradiances of 1.2 W/cm^2 and 0.6 W/cm^2 (beam diameters of 1 cm and 2 cm, respectively). Temperature variation was recorded using a thermocouple immersed in the medium at approximately 1 mm from the scaffold.

Control experiments were performed under identical conditions using PBS without scaffold. Additionally, PBS alone was irradiated at 10 W for 720 s, and temperature increase was monitored over the same duration. A control patch consisting of PBS with 5% CPX but without iron oxide nanoparticles (INPs) was also included. All experiments were conducted in triplicate, and results are reported as mean ± standard deviation. Temperature profiles were recorded and plotted as temperature versus time curves.

2.2.12. Differential Scanning Calorimetry (DSC)

DSC analyses were performed using a Setaram DSC131 EVO at a heating rate of 10 °C/min in the range of 25–350 °C, using nitrogen as a gas, and 120 μl aluminum non-hermetic crucibles. Pure drug, polymer,

physical mixture, and the scaffold were analyzed.

2.2.13. Mechanical characterization of the magnetic nano-electrospuns

Mechanical characterization of $PCI_{5\text{-}10}$ was performed by conducting uniaxial tensile-to-failure tests using a Bose TA Instruments ElectroForce Test Bench System. Rectangular specimens were obtained by cutting the scaffold along its longitudinal direction. The specimens had an average thickness of 0.37 mm, an overall length of 40 mm, and a width of 8 mm. The samples were clamped using mechanical grips with serrated contact surfaces, and the gauge length was set to 20 mm. Measurements were carried out in triplicate. Prior to testing, a preconditioning phase consisting of ten cycles at a frequency of 0.037 Hz and 1% strain was applied. The tensile test was then conducted under displacement control at a constant rate of 1 mm/min until specimen failure. Results were plotted as the following equations were used for data analysis:

$$\sigma\ (stress\ ) = \frac{streight\ [N]}{surface\ [m^2]}; \tag{4}$$

$$\varepsilon\ (strain) = \frac{L_f - L_i}{L_i} \tag{5}$$

$$E(Elastic\ modulus) = \frac{\sigma}{\varepsilon} \tag{6}$$

2.2.14. Evaluation of CPX release using Franz-type diffusion systems from the magnetic nano-electrospuns

CPX release experiments were carried out using vertical Franz-type diffusion cells, each equipped with an acceptor compartment filled with 5 mL of Dulbecco's phosphate-buffered saline (DPBS). A nanofibrous scaffold disk was placed in the donor compartment of one cell, while 1 mg of unformulated CPX was deposited onto filter paper in the donor compartment of a second cell, serving as a reference. The entire system was maintained at a constant temperature of 37 °C in a circulating water bath to simulate physiological conditions. Aliquots of 200 μL were withdrawn from the acceptor compartment at specified time intervals and immediately replaced with equal volumes of fresh DPBS to preserve sink conditions. UV-Vis spectroscopy was used for quantitative analysis of CPX in the samples. Upon completion of the release period, the residual CPX content in the scaffold materials was assessed. To this end, the remaining patches were dissolved in 2 mL of chloroform filtered through a 0.22 μm regenerated cellulose membrane and subjected to the same analytical procedures after filtration. Detection was carried out at 284 nm, CPX quantification was based on a linear calibration curve within the concentration range of 0.001–0.1 mg/mL (Fig. S4a of Supplementary Materials). All measurements were performed in triplicate to ensure statistical reliability. Release studies were also carried out under NIR irradiation, using the same experimental setup described for the CPX release, with vertical Franz cells. Specifically, the patch $PCI_{20\text{-}10}$ was irradiated for 5 days at 10 W for 400 s, followed by intermittent irradiation as previously described, for other 240 s; each day, 200 μL of medium were withdrawn and immediately replaced with an equal volume of fresh PBS. Collected samples were analyzed by a Jasco V760 UV–Vis spectrophotometer at 284 nm. Quantification was performed using a calibration curve generated from serial dilutions of a CPX standard solution, in PBS, of known concentration.

2.2.15. Iron species release studies from the magnetic nano-electrospuns

The release of INP and related species from the scaffold were evaluated in triplicate by placing approximately 5 mg of each patch into three separate vials, each containing 5 mL of PBS (pH 7.4). Aliquots of 150 μL were withdrawn at predetermined time points (24 h, 5 days, 10 days, 20 days, 30 days, 60 days, and 120 days) and replaced with an equal volume of fresh PBS to maintain constant volume and sink conditions. Each collected sample was treated with 50 μL of 6N HCl and incubated for 48 h. Iron quantification was performed using a colorimetric reagent based on phenanthroline method modified and measurements were conducted using an Eppendorf AF2200 plate reader at a wavelength of $\lambda = 540$ nm in a 96-well plate, as previously described for the iron loading assay (calibration curve is reported in Fig. S4b of Supplementary Materials).

2.2.16. Magnetic analysis of the magnetic nano-electrospuns

The magnetic response of the $PCI_{5\text{-}10}$ electrospun nanocomposite strip was investigated through a dual experimental approach. The first configuration employed a two-Hall-sensor setup to simultaneously monitor the applied magnetic field and the stray field generated by the sample. This arrangement was adapted and extended from the compact magnetometer methodology described by Ref. [59]. The second configuration utilized a fluxgate magnetometer, which offered higher sensitivity and stability in detecting weak magnetic signals [60]. The experimental design was guided by the established criteria for superparamagnetism, namely the absence of hysteresis, remanent magnetization, and coercive field [61]. Accordingly, the measurements focused on verifying the overlap of forward and reverse field sweeps and on confirming that the stray field tends to zero as the applied field approaches zero. By combining the comparative simplicity of the Hall-based setup with the enhanced resolution of the fluxgate technique, this work provides a preliminary study capable of evaluating the superparamagnetic behavior of the material.

2.2.16.1. Magnetic analysis based on Hall sensor. Hall sensors, widely used in several applications for monitoring magnetic field variations in their surroundings [62,63], are now employed to evaluate the magnetic response of the electrospun nanocomposite strip. The primary objective of this experiment was to replicate the methodology reported in previous studies while extracting key magnetic parameters, such as remanence and coercivity. The setup consisted of two permanent magnets arranged in a north–south configuration to generate a controllable external magnetic field. The sample was positioned at the center, between two Hall sensors (Figs. S5 and S6 of Supplementary Materials). One sensor monitored the applied magnetic field, while the other measured the stray field produced by the sample. This configuration allowed a direct comparison between the external field and the magnetic response of the material.

$$V_{0,A} = V_{0,B} = 2.5V$$

Sensors A and B exhibit a sensitivity of

SA=SB=19 mV/mT

as provided by the manufacturer. These parameters were used to convert the measured output voltages into corresponding magnetic field values, according to the relations defined in Equations (7) and (8). This ensured that the applied and stray magnetic fields were accurately quantified during the experiment.

$$B_{app} = \frac{(V_A - V_{0,A}) \times 10^3}{S_A} \tag{7}$$

$$B_{Stray} = \frac{(V_B - V_{0,B}) \times 10^3}{S_B} \tag{8}$$

To evaluate the material's response at different magnetic field strengths, the distance between the magnets and the sample was systematically varied. It was reduced from 55 mm to 30 mm in 5 mm steps (Fig. S7 of Supplementary Materials). At each distance, the voltages from both Hall sensors were recorded. To ensure reproducibility and to capture potential hysteresis effects, the procedure was repeated for both decreasing and increasing distance sweeps.

2.2.16.2. Magnetic analysis based on fluxgate magnetometer. To achieve higher performance in detecting weak magnetic responses and to focus

more specifically on aspects of interest in the material's response, the electrospun nanocomposite strip was also studied using a fluxgate magnetometer, which finds applications in various fields [64]. However, in the present case, the RTD-fluxgate system was employed to study the material's magnetic response, providing intriguing performance, including high sensitivity and high spatial resolution (approximately 100 μm) [65]. The enhanced sensitivity of the fluxgate magnetometer makes it particularly suitable for detecting subtle features, slopes, and nonlinearities in the magnetic response that are difficult to observe with Hall-effect sensors. However, due to its high sensitivity, the fluxgate is less suitable for measurements under strong magnetic fields and therefore serves as a complementary tool to the method described in the previous section. The operating principle of the fluxgate relied on the Residence Times Difference (RTD) method. In this technique, a periodic excitation current in the primary coil drives the ferromagnetic core into magnetic saturation. The resulting pulse-train response is then processed to extract information about the external magnetic field. The fluxgate sensor, mounted on a custom PCB with signal conditioning, recorded data via a National Instruments DAQ and LabVIEW. The sample (2 × 2 mm stacked squares) was measured in both orientations under a controlled magnetic field, with distances from 55 mm to 30 mm in 5 mm steps. This setup provided high-sensitivity validation of the sample's superparamagnetic behavior and stray field variations.

2.2.17. Biological characterization of the magnetic nano-electrospuns

2.2.17.1. Cell culture. Cell adhesion and proliferation assays were conducted using human gingival fibroblasts (HGF-1) and human epidermal keratinocytes (HaCaT). Cells were cultured in Dulbecco's Modified Eagle Medium (DMEM) supplemented with 10% fetal bovine serum (FBS), 4 mM L^{-1} glutamine, and 100 U/mL-100 μg/mL penicillin-streptomycin (referred to as complete DMEM). Actively proliferating cells in 75 cm^2 culture flasks were monitored using an inverted fluorescence microscope (Zeiss) equipped with a 5 × , 10 × , 15 × objectives. Cells were incubated at 37 °C in a 5% CO_2 atmosphere. When required, cells were centrifuged at 700×*g* for 5 min. For culture maintenance, the resulting pellet was re-suspended in an appropriate volume of fresh medium and seeded into new 75 cm^2 flasks at a split ratio of 1:5 or 1:8.

2.2.17.2. Cell viability assay. To assess the biocompatibility of PCI composite scaffolds, the Alamar Blue (AB) assay was performed. HGF-1 and HaCaT cells were seeded at a density of 10,000 cells per well in 48-well plates. Patches approximately 12 mm in diameter were secured within CellCrown™ by Scaffdex inserts and placed in contact with the cells using 450 μL of DMEM. The cells were incubated under standard culture conditions until the AB assay was carried out, following the manufacturer's instructions. Briefly, prior to the assay, the medium and CellCrown™ inserts were removed, and cells were gently rinsed with PBS. Then, 350 μL of a 10% (v/v) AB solution, prepared in fresh medium without FBS or supplements, was added to each well. After 3 h of incubation, 150 μL of the solution was transferred to a 96-well black fluorescence plate with V-bottom wells, and fluorescence was measured at excitation/emission wavelengths of 530/590 nm using an Eppendorf AF2200 microplate reader. Cell viability was assessed after 24 and 48 h of incubation with the scaffolds. Results were averaged over three replicates and reported as mean ± standard deviation. Fluorescence values were normalized to those obtained from wells containing AB solution with cells and without scaffolds (positive control). Wells containing only AB solution without cells were also included as blanks, and their fluorescence values were subtracted as background.

2.2.18. Statistical analysis

Statistical analysis was performed in particular on cytocompatibility study, using one-way analysis of variance (ANOVA) followed by Holm–Šidák multiple comparisons test. Statistical calculations were performed using the Microsoft®-Excel, OriginPro 8.5. and the software package GraphPad Prism (V.7.03).

3. Results and discussions

3.1. Production of the magnetic nano-electrospuns

Electrospun scaffolds based on PBS, CPX, and INPs were successfully fabricated through a one-step process, yielding uniform and defect-free fibrous mats. To better understand the effects of magnetite content on the biopolymer's properties and to assess the potential of the scaffold as a drug delivery system, we carried out the present studies on three scaffold formulations with varying concentrations of magnetite and CPX, as detailed in Table 1. The electrospinning conditions were developed and optimized using the MECC NF 104 electrospinning prototyping system, which enabled a straightforward and highly reproducible setup process. The prototyping device allowed us to quickly and easily modify certain parameters and produce small prototypes useful for evaluating the impact of variables on the final characteristics of the electrospun material. Final parameters were selected because they allow the production of a strong biomaterial made of thin, defect-free fibers. We observed that increasing the voltage affects fiber dimensions, and higher voltages result in thinner fibers. Fiber size is also influenced by the flow rate, with higher flow rates producing fibers of larger diameter. However, since the aim of this work was not to investigate the influence of spinning parameters on the characteristics of the resulting material, we limited ourselves to obtaining a material with the desired features, mainly the absence of defects and small fibers capable of enhancing the properties of nanostructured materials. For this reason, after a few preliminary tests, we optimized the parameters and used them to produce all the scaffolds used in this study, namely: feed rate 0.8 mL/h, voltage 15 kV, volume 5 mL, needle-to-collector distance 10 cm, collector rotation speed 250 rpm, traverse speed 20 mm/s, traverse distance 120 mm.

The most critical phase of optimization was achieving a sufficiently stable suspension of the three components (polymer, antibiotic, and nanoparticles) to minimize precipitation inside the syringe during electrospinning. While both PBS and CPX are soluble in HFIP, the nanoparticles are not readily dispersible. To improve the stability of the suspension, CPX was first dissolved in HFIP along with the polymer. Once complete solubilization was achieved, INP was added and dispersed using orbital shaking and vortexing. This initial procedure led to scaffolds with low iron loading efficiency (15–20%) due to partial precipitation of the nanoparticles within the syringe. To enhance loading efficiency and ensure complete nanoparticle suspension, we conducted a preliminary qualitative visual study of sedimentation and time-dependent phase separation (Figs. S1 and S2 of Supplementary Materials), based on these findings, we ultimately adopted the following protocol: the mixture was subjected to alternating 30 min cycles of vortex agitation and sonication. Stability was monitored through simple visual phase separation tests. With vortexing alone, sedimentation began in under an hour, and a clear phase separation was visible within

Table 1
Composition of PCI electrospun scaffolds (15% w/v PBS) showing theoretical and experimentally determined loadings of ciprofloxacin (CPX) and iron oxide nanopowder (INP). Experimental values are reported as mean ± standard deviation (n = 4).

Name	PBS content	CPX theoretical content	CPX experimental content	INP theoretical content	INP experimental content
$PCI_{5\text{-}5}$	15% p/v	5% p/p	5.1 ± 0.4%	5% p/p	2.6 ± 1.3%
$PCI_{5\text{-}10}$	15% p/v	5% p/p	4.8 ± 0.6%	10% p/p	2.4 ± 1.2%
$PCI_{20\text{-}10}$	15% p/v	20% p/p	19.8 ± 0.3%	10% p/p	3.8 ± 1.5%

a couple of hours. By using alternating agitation and sonication over an optimized period of 3 h, followed by overnight agitation and a final hour of sonication just before electrospinning, we were able to obtain a stable suspension at 25 °C for up to 5 h, which is compatible to the time used in spinning protocol. This improved process resulted in significantly higher iron encapsulation efficiency (~40-50%). Iron loading measurements yielded 2.6 ± 1.3% (significancy) for $PCI_{5\text{-}5}$, with an encapsulation efficiency of ~52%, 2.4 ± 1.2% for $PCI_{5\text{-}10}$, with an encapsulation efficiency of ~48% and 3.8 ± 1.5% for $PCI_{20\text{-}10}$, with an encapsulation efficiency of ~38%. These values, as for CPX, were determined from four about 10 mg samples punched from different areas of each patch. The concentration of ciprofloxacin detected was even more homogeneous, with a drug content (DL%) of 5.1 ± 0.4% and 100% loading efficiency for $PCI_{5\text{-}5}$, 19.8 ± 0.3% and 99% loading efficiency for $PCI_{20\text{-}10}$. These findings confirm that electrospinning allows a partial incorporation of the added INP and complete encapsulation of CPX. The higher loading efficiency of CPX compared to INP is attributable to its full solubility in the polymeric blend, whereas the nanoparticles tend to partially precipitate, an effect that becomes more pronounced at higher concentrations as highlighted from nanosponges EC values comparation. By comparing drug and iron loading and loading efficiency, it can also be observed that the patches are very uniform in their CPX content (due to the very low standard deviation of the values) and slightly less so in their INP content. This observation is also related to the complete solubilization of CPX in the spinning mixture, as opposed to a dispersion of INP.

3.2. Morphological characterization of the magnetic nano-electrospuns

The resulting scaffolds exhibited a defect-free fibrous morphology. Under the optimized spinning conditions, the following fiber diameters were obtained: **153 ± 29.03 nm** for PCI5-5, **159.13 ± 26.34 nm** for PCI5-10, and **160 ± 26.55 nm** for PCI20-10.

Fig. 1 shows diameters distribution and SEM micrographs of the three nanofibrillar mats. The average fiber diameters were similar across all formulations, indicating that variations in the components concentrations had a minimal impact on fiber size.

SEM analyses achieved without gold sputtering show the presence of small iron particles, visible as bright spots, good distributed along the fibers. EDX analysis confirms that these are iron particles, results are represented in Fig. 2.

Micro-CT analysis confirmed the X-ray detectability of iron oxide nanopowder (INP), enabling detailed investigation of the internal structure of the scaffolds and accurate measurement of sample thickness. The analysis also highlighted the presence of high-attenuation domains within the fibrous matrix, which may be interpreted as micro-sized aggregates of nanoparticles. However, it is important to note that the apparent size and contrast of such features can be influenced by micro-CT imaging and reconstruction effects, including beam hardening and partial volume phenomena, potentially leading to an overestimation of aggregate dimensions. In this context, SEM observations revealed a homogeneous fibrous network with nanoparticles appearing as well-dispersed bright domains along the fibers, without evidence of large-scale or micron-sized aggregation. This suggests that the features observed in micro-CT (Fig. 3a and b) may be partially amplified by imaging contrast rather than reflecting extensive nanoparticle clustering. Importantly, regardless of the origin of these features, no detrimental effects on the functional properties of the scaffolds were observed. Despite partial aggregation or apparent clustering, functional performance was preserved, as demonstrated by the maintained superparamagnetic behavior, stable NIR-induced photothermal response, and reproducibility over time. From a biological perspective, the embedding of nanoparticles within the polymeric matrix likely limits their mobility, reducing potential safety concerns, as further supported by the absence of iron release and the high cytocompatibility observed.

3.3. Physical-chemical characterization of the magnetic nano-electrospun

Contact angle measurements showed that all three scaffolds were completely wettable, as the water droplet was absorbed immediately, allowing the formation of only a very small angle. This behavior was previously observed for PBS–CPX scaffolds [55] but not for pure PBS patches. Fig. 4 shows the behavior of $PCI_{5\text{-}5}$ vs PBS alone. These results suggest that the incorporation of CPX can alter the surface properties of PBS electrospun mats, enhancing their hydrophilicity and wettability.

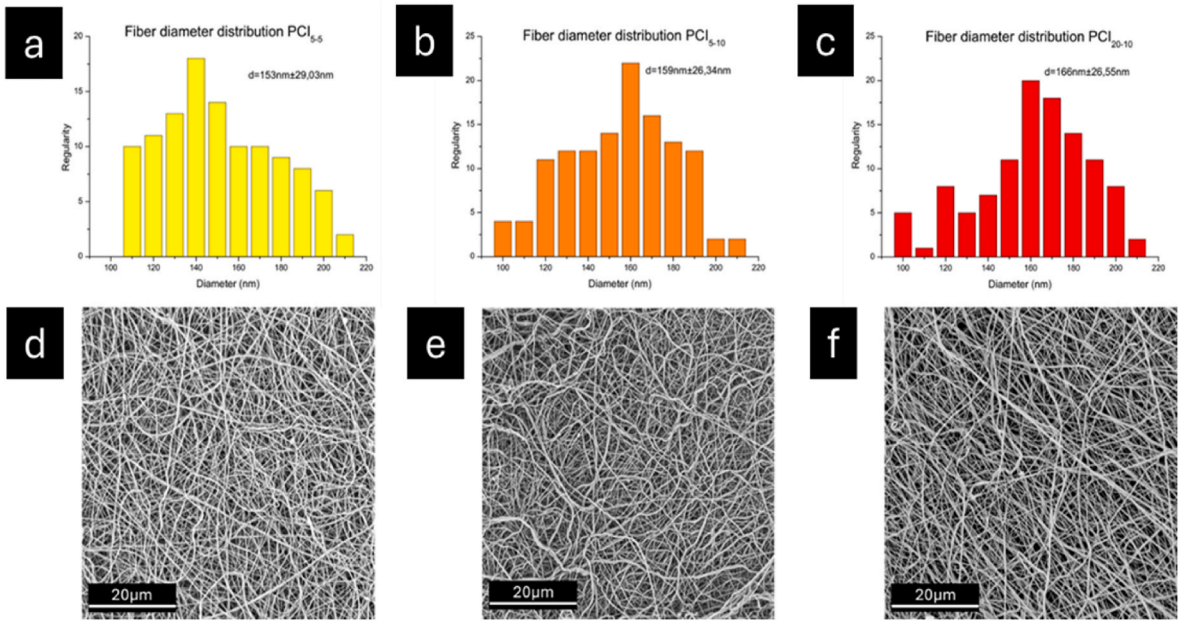

Fig. 1. Morphological characterization and fiber diameter distribution of electrospun PCI scaffolds with increasing nanoparticle/drug loading: (a-c) Histograms of fiber diameter distribution for $PCI_{5\text{-}5}$, $PCI_{5\text{-}10}$ and $PCI_{20\text{-}10}$ formulations, showing mean diameters of 153 ± 29.03 nm, 159 ± 26.34 nm, and 166 ± 26.55 nm, respectively. A slight increase in average fiber diameter is observed with higher nanoparticle/drug content, while maintaining a relatively narrow distribution. (d-f) Corresponding SEM micrographs reveal homogeneous, bead-free fibrous networks with random orientation. The incorporation of magnetic nanoparticles and ciprofloxacin does not significantly alter fiber morphology, confirming the robustness of the electrospinning process. Scale bar: 20 µm.

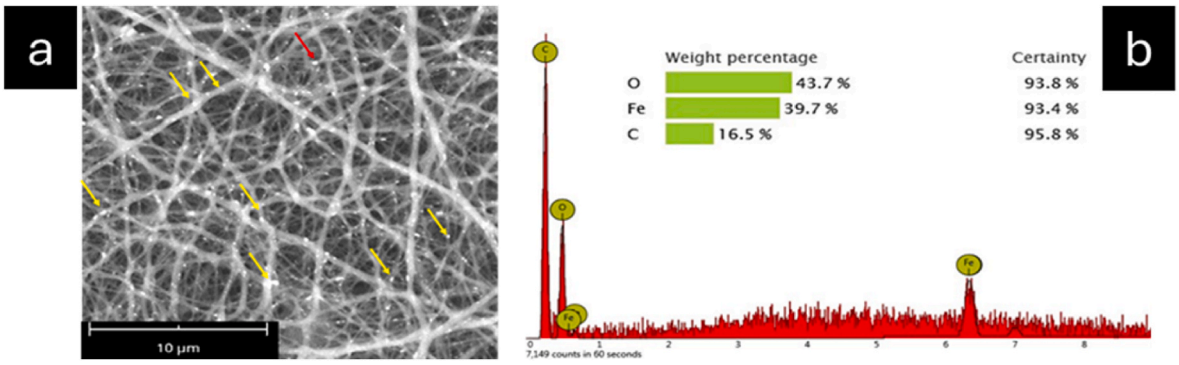

Fig. 2. Morphological and compositional analysis of $PCI_{5\text{-}10}$ electrospun scaffold: (a) SEM micrograph of non-gold sputtered PCI_{5-10} fibers, highlighting the presence of embedded iron oxide nanoparticles visible as bright spots (yellow arrows), homogeneously distributed within the fibrous network. Red arrows indicate the locations selected for EDX analysis. (b) Corresponding EDX spectrum and elemental quantification confirm the presence of Fe consistent with the successful incorporation of iron oxide nanoparticles within the polymeric matrix. (For interpretation of the references to color in this figure legend, the reader is referred to the Web version of this article.)

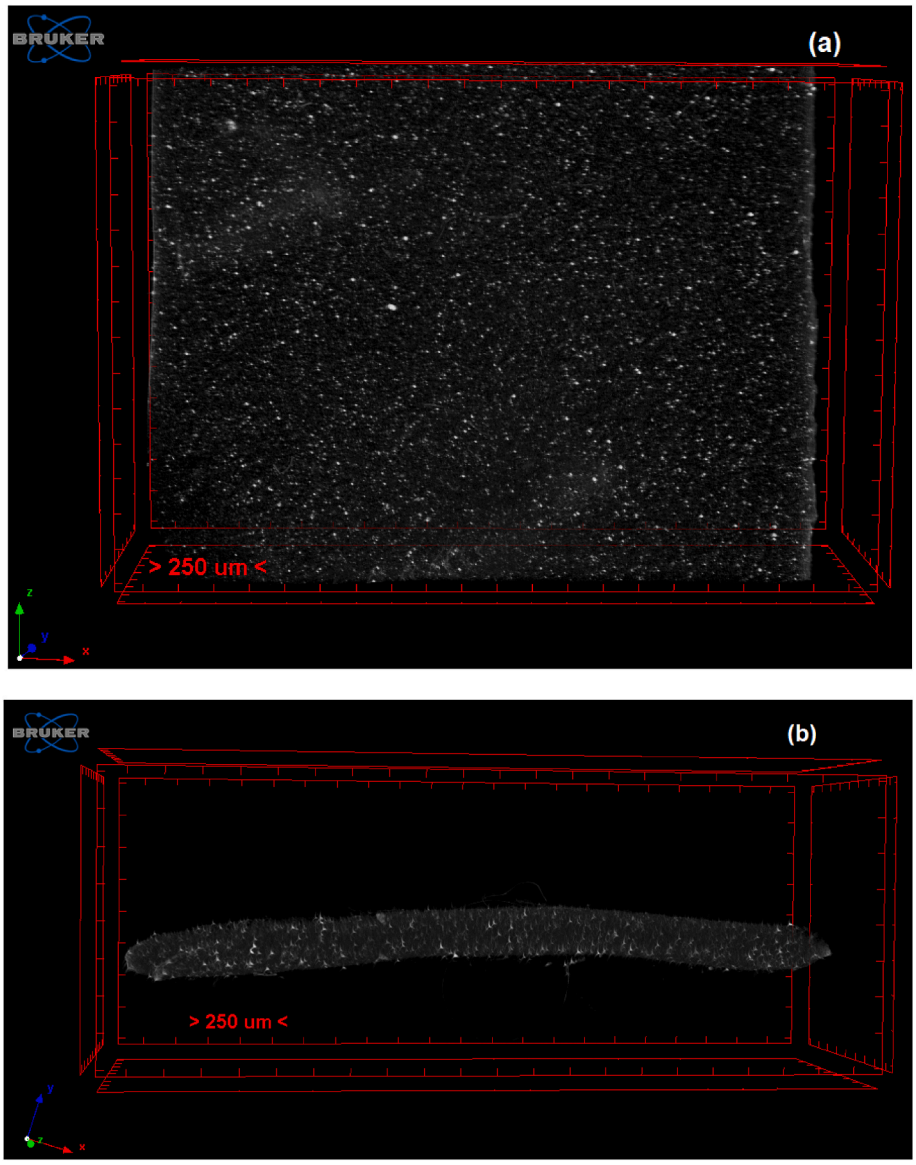

Fig. 3. Micro-computed tomography (micro-CT) 3D reconstructions of $PCI_{5\text{-}10}$ electrospun scaffolds: (a) Top view demonstrating the homogeneous distribution and X-ray detectability of iron oxide nanopowder (INP) within the fibrous matrix. (b) Cross-sectional reconstruction revealing the internal architecture and enabling precise thickness measurement, with values ranging from 175 to 207 µm. Micron-sized nanoparticle aggregates are visible within the matrix.

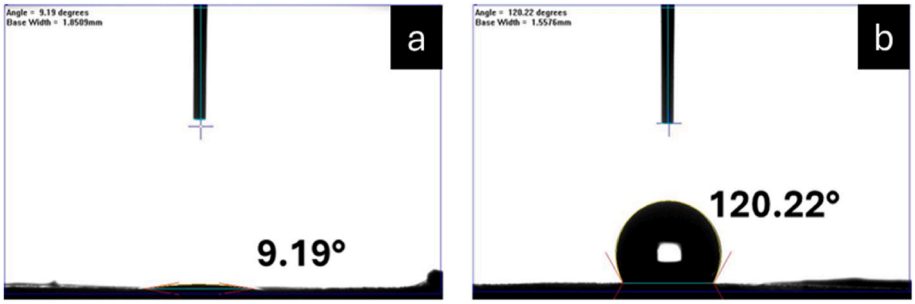

Fig. 4. Wettability assessment of electrospun scaffolds: (a) Static water contact angle measurement of $PCI_{20\text{-}10}$ showing a highly hydrophilic behavior (9.19°), indicative of enhanced surface wettability due to the incorporation of iron oxide nanoparticles and ciprofloxacin. (b) Contact angle of neat PBS electrospun scaffold, exhibiting hydrophobic behavior (120.22°). The marked reduction in contact angle for PCI_{20} $PCI_{20\text{-}10}$ highlights the significant modification of surface properties, which may promote improved biological interactions.

These observations were further supported by water uptake studies comparing PBS and $PCI_{20\text{-}10}$ with similar thickness (Fig. 5). After 24 h, the PBS scaffold showed a 130% increase in weight (equivalent to retaining approximately 2.3 times its dry weight in water), while $PCI_{20\text{-}10}$ showed a 300% increase (approximately 4 times its dry weight). These findings highlight the enhanced hydrophilic nature of PCI electrospun scaffolds relative to pure PBS.

The WVTR, measured for $PCI_{5\text{-}10}$ and $PCI_{20\text{-}10}$, increased linearly, but after about 15 min for all, the value gains a plateau. Fig. 5 shows the outstanding WVTRs after 15 min. For PCI $_{5\text{-}10}$ at 25 °C, 6721.239 ± 93.573 g/m^2 x 24h and 13598.634 ± 109.521 g/m^2 x 24h at 38 °C; and for PCI $_{20\text{-}10}$ 6802.239 ± 107.83 g/m^2 x 24h at 25 °C and 13311.681 ± 87.32 g/m^2 x 24h at 38° = = C.

The WVTR values obtained for the tested patches do not differ significantly from each other, and from the values previously reported for the PBS-CPX 20% patch (6869.87 ± 154.37 g/m^2 × 24 h at 25 °C and 13,598.63 ± 169.52 g/m^2 × 24 h at 38 °C), which was prepared by our research group [55]. The WVTR values measured for a scaffold composed solely of PBS were 6859.65 ± 109.78 g/(m^2 × 24 h) and 13,906.74 ± 121.45 g/(m^2 × 24 h).

These results suggest that the breathability of the material is primarily conferred by the base polymer (PBS), and that the incorporated substances, in this case, CPX and INP, have no effect on this property. Biomaterials with a high-Water Vapor Transmission Rate are particularly valuable in biomedical applications, as they promote wound healing by maintaining a moist environment while preventing tissue maceration and by keeping the wound hydrated and promoting better healing, can lead to less pain and improved cosmetic outcomes [66]. In transdermal patches, they help minimize skin moisture accumulation, thereby improving both comfort and adhesion. In tissue engineering scaffolds, high WVTR supports gas exchange and cellular viability. Additionally, in wearable medical devices and prosthetics, such materials enhance breathability, and improve long-term user tolerability.

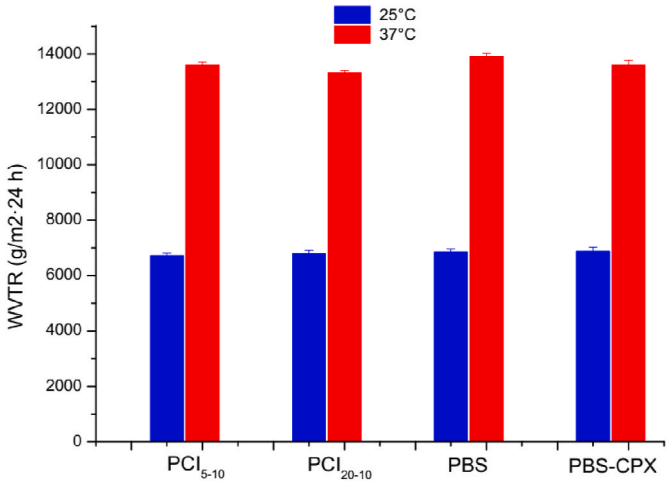

Fig. 5. Water vapor transmission rate (WVTR) of electrospun scaffolds: $PCI_{5\text{-}10}$, $PCI_{20\text{-}10}$, PBS and PBS-CPX measured at 25 °C (blue) and 37 °C (red) for $PCI_{5\text{-}10}$, $PCI_{20\text{-}10}$, PBS, and PBS-CPX samples. All formulations exhibited increased WVTR values at physiological temperature, indicating enhanced vapor permeability. Comparable WVTR values were observed among the different scaffold compositions, suggesting that the incorporation of CPX and INPs does not significantly affect vapor transport properties. Data are presented as mean ± standard deviation (n = 3) thickness of the samples from 172 nm to 188 nm. (For interpretation of the references to color in this figure legend, the reader is referred to the Web version of this article.)

Attenuated total reflection Fourier transform infrared spectroscopy (FTIR-ATR) analysis of the magnetic nanofibrous mats were acquired to investigate their surface structure. The IR signals of ciprofloxacin, previously assigned in the literature [67,68], were also identified in our spectra. In particular, the characteristic band corresponding to the n (C=O) vibration of the carboxylic group in ciprofloxacin is at 1707 cm^{-1} [66]. In the IR spectra of ciprofloxacin reported, there are no analogous peaks due to the deprotonation of COOH group [68]. Some authors have pointed out that ionic carboxylates show no carbonyl band around 1700 cm^{-1}, but instead have two absorption bands due to the asymmetric (n_{as}(O–C–O)) and symmetric(n_s(O–C–O)) stretching vibrations that occur in the ranges 1610–1580 cm^{-1} and 1400–1280 cm^{-1}, respectively. Here, a distinct peak at 1622 cm^{-1}, characteristic of CPX carboxylate, is clearly observed in both $PCI_{5\text{-}10}$ and $PCI_{20\text{-}10}$ samples, with a noticeable increase in intensity corresponding to the higher ciprofloxacin content (from 5% to 20%) in the nanosponges (Fig. 6a and b). It is difficult, however, to assign unambiguously these vibrations in the spectra of quinolones on account of the numerous other bands present in these regions, so only the region from 1800 to 1500 cm^{-1} is considered diagnostic to this aim here. Bands at 1586 and 1377 cm^{-1} are attributed to the asymmetric and symmetric stretching vibrations of the deprotonated carboxylate group, respectively [69]. The peaks in the PBS spectrum at 1716 and 1155 cm^{-1} correspond to carbonyl and –C–O–C– stretching in ester linkage, respectively. Moreover, the band at 1045 cm^{-1} is due to –O–C–C– stretching vibrations in PBS [70]. The coupled deformation of the C-C(C=O)-O group from ester shows up at 1331 and 955 cm^{-1} [71]. All the peaks mentioned above can also be found in the spectrum of the analyzed scaffolds, confirming their incorporation. FTIR analysis indicates that ciprofloxacin is present at the surface of the PCI mats, predominantly through its carboxylic group in the deprotonated form. This surface localization likely accounts for the increased hydrophilicity of CPX-loaded electrospun fibers compared with neat PBS mats, as evidenced by contact angle measurements and water uptake studies. The same molecular features may also explain the role of CPX in promoting fiber formation during electrospinning. The presence of ionizable functional groups facilitates charge generation under the applied electric field, increasing the electrical conductivity of

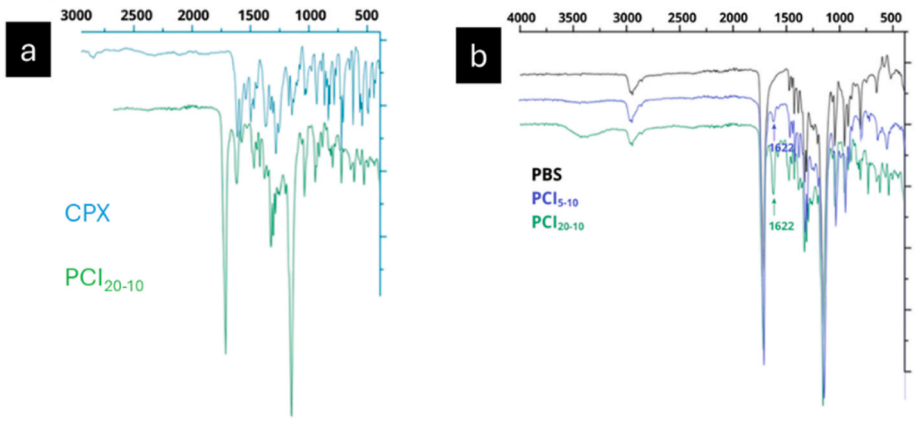

Fig. 6. FTIR-ATR analysis of CPX-loaded electrospun scaffolds: (a) FTIR-ATR spectra of ciprofloxacin (CPX) and $PCI_{20\text{-}10}$ confirming the presence of characteristic CPX absorption bands within the composite scaffold. (b) Comparative spectra of PBS, $PCI_{5\text{-}10}$, $PCI_{20\text{-}10}$. The band at 1622 cm^{-1}, attributed to the asymmetric stretching of the deprotonated carboxylate group ($–COO^-$) of CPX, is highlighted. Its intensity increases progressively with CPX loading, confirming the successful incorporation of the drug within the electrospun fibers. No significant peak shifts are observed, suggesting the absence of strong chemical interactions and indicating that CPX is physically embedded within the polymeric matrix.

the spinning solution and improving jet stability. At the same time, the lipophilic portion of the fluoroquinolone structure can interact with the hydrophobic PBS matrix, favoring drug retention within the fibers. Overall, FTIR-ATR results suggest a preferential orientation of the carboxylic groups toward the fiber surface, supporting partial surface exposure of CPX within the electrospun scaffold. Moreover, as previously discussed, the presence of ciprofloxacin at the fiber surface is responsible for the new functional properties imparted to the PCI scaffolds, rendering them more wettable compared to the neat PBS matrix. At the same time, it accounts for the enhanced water uptake capacity observed in the CPX-containing mats. In conclusion, it is evident that the addition of CPX to the spinning solution increases the hydrophilicity of the resulting electrospun mats, as supported by multiple experimental findings.

The thermal behavior of the scaffold was evaluated by Differential Scanning Calorimetry (DSC). The analysis was performed on starting polymer (PBS), CPX, the $PCI_{20\text{-}10}$ scaffold, and the physical mixture of the first three ones (Fig. 7). The thermogram of PBS shows a distinct melting point at 118 °C, with a sharp endothermic peak indicating a crystalline structure of the polymer [72]. CPX, which is also crystalline, exhibits a well-defined melting peak at 271.8 °C [73]. The physical mixture displays both melting peaks of the individual components, with a slight shift in the CPX melting peak (263.58 °C), likely due to minor interactions occurring during the preparation of the mixture. In contrast, the scaffold thermogram shows only the PBS melting peak, with no detectable CPX peak, this behavior can be explained by two phenomenas: CPX undergoes an amorphization process that alters its thermal characteristics during the electrospinning process [55] and a large amount of CPX can be entrapped in polymer fiber maybe in solid solution that modify melting point temperature. The thermogram of iron oxide (not shown) does not display any characteristic peaks below 500 °C.

Mechanical characterization of magnetic nanofibrous mats was carried out only on $PCI_{20\text{-}10}$ as model sample. The analysis of data obtained from preliminary mechanical testing of the scaffold $PCI_{20\text{-}10}$ revealed that the biomaterial initially exhibits a linear behavior, in which stress is proportional to strain, following Hooke's law. As the applied stress increases, the material undergoes plastic deformation. The Young's modulus, calculated from triplicate measurements as the slope of the linear region of the stress–strain curve, was 19.38 ± 1.94 MPa. The maximum tensile strength (σ max) was 2.96 ± 0.30 MPa, and the maximum strain (ε max) was 30.25 ± 3.02%. These results indicate that the scaffold possesses mechanical properties suitable for biomedical applications, as that its Young's modulus is higher than that of tendons and cartilage [74].

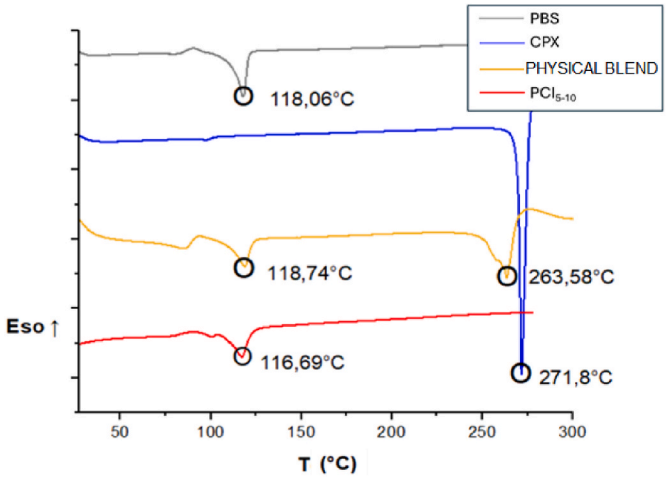

Fig. 7. Differential scanning calorimetry (DSC) thermograms of PBS, ciprofloxacin (CPX), physical blend, and PCI scaffold: Thermograms of neat PBS, CPX, their physical mixture, and PCI scaffold are reported. PBS exhibits its characteristic melting temperature around 118 °C, which is preserved in both the physical blend (118.74 °C) and $PCI_{5\text{-}10}$ scaffold (116.69 °C), indicating that the polymer crystalline structure is not significantly altered by electrospinning or loading. CPX shows a sharp endothermic peak at ~271.8 °C, associated with its melting/decomposition. This peak is clearly visible in the physical mixture (~263.6 °C) but is absent in the PCI scaffold, suggesting that CPX is molecularly dispersed or present in an amorphous state within the electrospun fibers.

3.4. *Responsiveness of the magnetic nano-electrospun to external stimuli*

Notably, the use of iron oxide as a photothermal agent in electrospun systems is still scarcely reported, making this approach particularly relevant in the context of stimuli-responsive biomaterials. This aspect, combined with the use of dry nanopowder instead of stabilized dispersions, further distinguishes the proposed system from conventional photothermal electrospun platforms.

3.4.1. Heating studies under NIR irradiation and magnetic resonance images (MRI) of the mats

Irradiation studies using near-infrared (NIR) light confirmed that PCI patches are responsive to NIR stimulation. While patches previously prepared without iron oxide nanoparticles (INPs) did not show relevant heating under NIR exposure and behaved similarly to phosphate buffer pH 7.4 (used as blank) under the experimental conditions using for PCI test (Fig. 8a).

Upon irradiation at 10 W power using an irradiance density of 51.02W/cm^2, the PCI5$_{-5}$ and PCI$_{20\text{-}10}$ patches exhibited a concentration dependent heating response: the greater the INP content, the higher the temperature increase. As shown in Fig. 8b, both patches reached a thermal plateau after approximately 20 min (1200 s), beyond which no further increase in temperature was observed under the experimental setup. Specifically: PCI$_{5\text{-}10}$ increased from 25 ± 0.2 °C to 38.3 ± 0.3 °C after 1200 s (ΔT = 13.3 °C), PCI$_{20\text{-}10}$ increased from 25 ± 0.2 °C to 42 ± 0.5 °C after 1200 s (ΔT = 17 ± 0.3 °C). Additional experiments were conducted at a starting temperature of 37 °C using only PCI$_{20\text{-}10}$ (Fig. 8c) selected for its superior performance and major drug loading. Under these conditions, the patch reached 42 °C (ΔT = 5 °C) in approximately 7 min, indicating a slower heating rate at higher starting temperatures. In comparison, when irradiated from 25 °C, the same patch reached 36.5 °C (ΔT = 11.5 °C), confirming the dependence of heating dynamics on the initial temperature. Finally, we investigated whether the target temperature of 42 °C could be maintained using pulsed rather than continuous NIR irradiation. After optimization, a pulsing regimen of 12 s ON and 10 s OFF successfully sustained the temperature at 42 °C for the entire duration of the experiment (16 min, maximum tested time) as shown in Fig. 8d.

Additional NIR irradiation experiments were performed under lower irradiance conditions using the PCI$_{20\text{-}10}$ formulation, selected as the patch with the highest iron and drug content (Fig. 9a). At an irradiance of 1.2 W/cm^2, the temperature increased from 37 °C to approximately 43.5 °C within 300 s, reaching a near plateau. At 0.6 W/cm^2, the temperature increased from 37 °C to approximately 40.7 °C within 500 s, also approaching a plateau. Control experiments performed with PBS alone showed negligible temperature variation under the same conditions.

These results confirm that PCI$_{20\text{-}10}$ exhibits a measurable photothermal response even at lower irradiance levels, with a temperature increase dependent on the applied irradiation conditions.

Notably, the ability of the PCI$_{20\text{-}10}$ patch to reach a temperature of approximately 43 °C at an irradiation power of 1.2 W/cm^2 appears higher than that observed at 51 W/cm^2. This seemingly counterintuitive result can be attributed to differences in the experimental setup. Specifically, the measured temperature reflects the heating of the surrounding medium in which the patch is immersed and is strongly influenced by both the buffer volume and the distance between the patch and the thermocouple. In the low-irradiance experiments, the volume of PBS was significantly smaller (2 mL) compared to that used under high-power conditions (10 mL), and the thermocouple was positioned much closer to the sample (approximately 2 mm vs 2.5 cm). These factors result in a more pronounced apparent temperature increase. The photothermal performance of the PCI system was compared

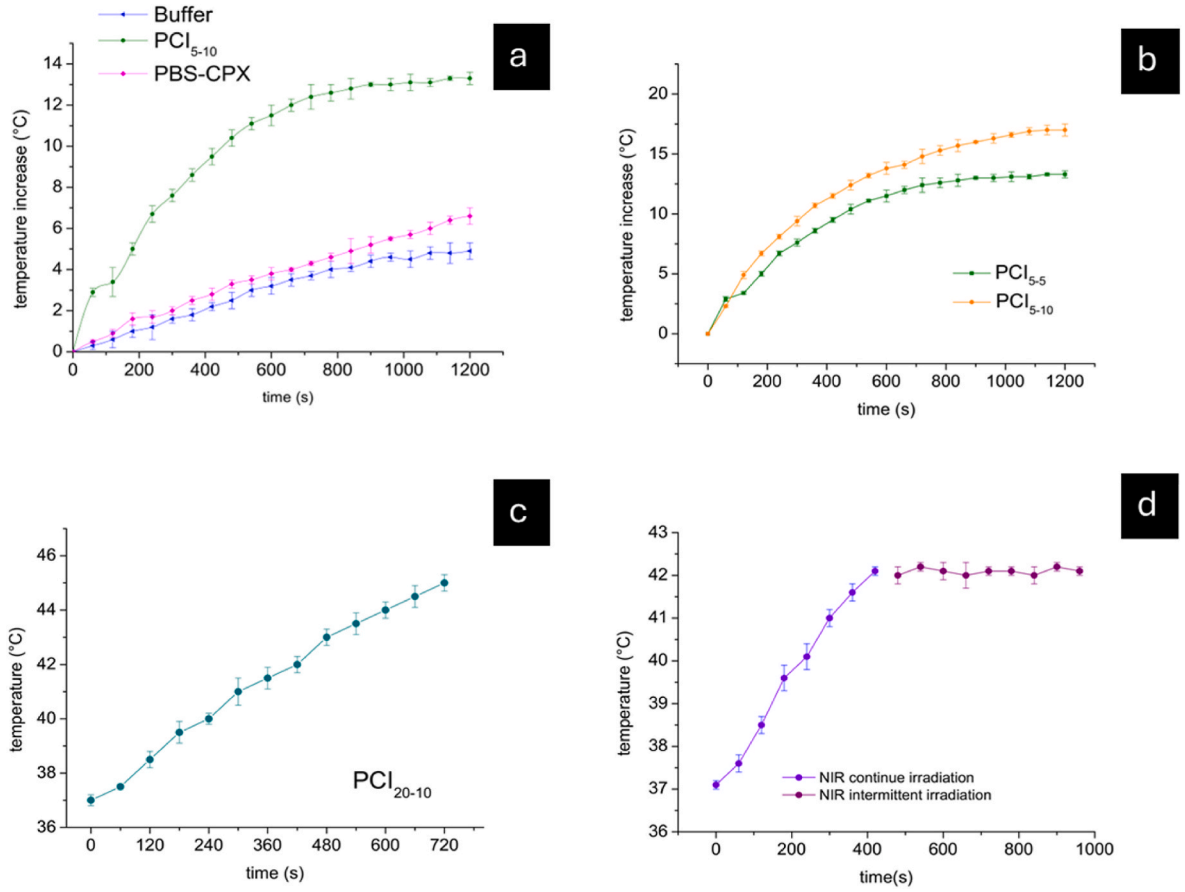

Fig. 8. Photothermal performance of PCI scaffolds under NIR irradiation (10 Watt): (a) Temperature increase over time for PCI$_{5\text{-}10}$ compared to PBS–CPX and buffer controls. PCI$_{5\text{-}10}$ exhibits a significantly higher temperature rise, confirming the effective photothermal conversion induced by iron oxide nanoparticles. (b) Comparison between PCI$_{5\text{-}5}$ and PCI$_{5\text{-}10}$ shows a concentration-dependent photothermal response, with higher nanoparticle/drug loading leading to increased temperature elevation. (c) Absolute temperature profile of PCI$_{20\text{-}10}$, reaching ~45 °C under NIR irradiation. (d) Heating behavior under continuous and intermittent NIR irradiation demonstrates good photothermal stability and reproducibility, with negligible thermal decay during cycling.

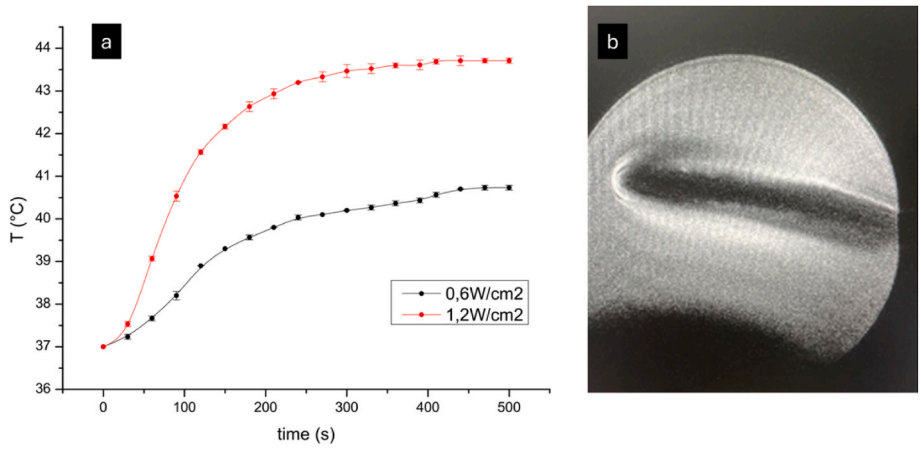

Fig. 9. Photothermal response and magnetic resonance imaging capability of PCI scaffolds at low irradiance density: (a) Temperature profiles of PCI_{20-10} under NIR irradiation at two irradiance levels (0.6 and 1.2 W/cm^2), achieved by varying the beam spot size at constant power (1 W), in PBS (pH 7.4). PCI_{20-10} exhibits a power density–dependent heating, reaching ~40.7 °C and ~43.5 °C, respectively, while PBS alone shows negligible temperature variation. Data are reported as mean ± SD (n = 3). (b) Magnetic resonance image of PCI_{5-10}, demonstrating its contrast capability due to the presence of iron oxide nanoparticles.

with previously reported photothermal platforms, including mGelMx nanofiber films [75] and PCL/TA/Fe^{3+} nanofiber membranes [14]. At first glance, the temperature increase achieved by PCI (ΔT ≈ 6.5 °C, from 37 to ~43.5 °C in 300 s at 1.2 W/cm^2) appears lower than that reported for mGelMx systems, which reached temperature increases of approximately 25–30 °C within 2–4 min at 1 W/cm^2. However, this comparison is influenced by the significantly different experimental volumes (2 mL in this study vs 0.5 mL in the literature), which affect the apparent temperature rise due to differences in thermal capacity. When qualitatively accounting for this factor, the photothermal performance of the PCI system can be considered comparable to that of mGelMx-based platforms. A more direct comparison can be established with PCL/TA/Fe^{3+} nanofiber membranes, which exhibited a temperature increase of approximately 8 °C after 5 min of irradiation under similar conditions, reaching values slightly above 44 °C at higher power densities. In this context, the PCI system shows a comparable photothermal response, despite being tested in a larger volume and under physiologically relevant starting conditions (37 °C). Importantly, all systems achieve temperature ranges associated with mild hyperthermia (~42–45 °C), which is considered optimal for antibacterial activity and wound healing applications while minimizing thermal damage to surrounding tissues. In contrast, higher temperature increases, such as those observed for mGelMx systems (>50 °C), may not be ideal for in vivo applications due to potential cytotoxic effects.

Overall, the PCI platform demonstrates an efficient and controlled photothermal behavior under more demanding experimental conditions, combining effective temperature elevation with a safer and more translationally relevant thermal profile. This suggests that the patch likely reached local temperatures higher than those measured in the bulk medium, exceeding the equilibrium temperature with water. A magnetic resonance image presented in Fig. 9b was acquired to demonstrate the practical feasibility of detecting, controlling, and monitoring a potential PCI implantation in vivo. Such imaging capability enhances the scientific and clinical relevance of PCI-based systems, making their application as implantable biomaterials particularly promising.

3.5. Release studies

The incorporation of iron oxide into the scaffold for biomedical applications may pose the potential drawback of in vivo release of the substance from the fibrous patch, leading to a loss of the material's magnetic properties. To assess potential iron release, an appropriately sized and accurately weighed scaffold disc was incubated in phosphate buffer (pH 7.4) at 37 °C. Samples of the incubation medium were collected at predetermined time intervals for up to 3 months. Iron oxide release was quantified using a spectrophotometric method analogous to that used for the experimental determination of iron loading. The results indicate that no detectable iron release occurred over the 30 days monitoring period. These findings were further confirmed by quantitative analysis of residual iron on the patch at the end of the experiment, performed after scaffold dissolution in acidic conditions. The residual experimental iron loading was found to be comparable to that of scaffolds not subjected to the release study. The absence of iron release from the material suggests that the properties imparted by the nanoparticles, such as photoactivated drug release and heating capability under NIR light, remain stable for at least 30 days, even during material implantation or upon contact with skin or physiological fluids.

3.5.1. *Evaluation of CPX release using Franz-type diffusion system with and without NIR irradiation*

To assess the ability of the material to release a drug, with and without photostimulation, the electrospun scaffold was pre-loaded with a model drug. Ciprofloxacin (CPX), a fluoroquinolone antibiotic, was selected for this purpose due to several advantages. CPX has a high molar extinction coefficient about 3700 λ/Mcm (experimentally calculated from the Lambert-Beer law equation), which allows for easy detection at very low concentrations using UV spectroscopy (Fig. S2a); its incorporation improves the morphological features of the electrospun material, enabling the consistent formation of defect-free fibers across a wide range of spinning conditions; finally, CPX has been previously used in earlier studies conducted by our research group.

We investigated the release of CPX from two PCI scaffolds containing 5% and 20% CPX, both also incorporating 10% INP. Experiments were carried out using Franz diffusion cells in phosphate buffer (pH 7.4) and release graphs are shown in Fig. 10. Comparative release tests between PCI_{5-10} and PCI_{20-10} revealed that approximately 70% of the drug was released from PCI_{5-10} within the first hour, with nearly complete release (≈100%) achieved within 5–6 h. In contrast, the release profile from PCI_{20-10} was significantly more prolonged and therefore of greater interest. For this reason, PCI_{20-10} was used for comparative drug release studies with and without NIR irradiation.

These experiments were designed to determine whether and how photostimulation with near-infrared (NIR) light affects drug release. In initial Franz cell studies without NIR exposure, approximately 40% of the loaded CPX was released over 11 days. The experiment was concluded at this point, as the release had reached a plateau, indicating completion. Thus, at a 20% concentration, CPX is released very slowly,

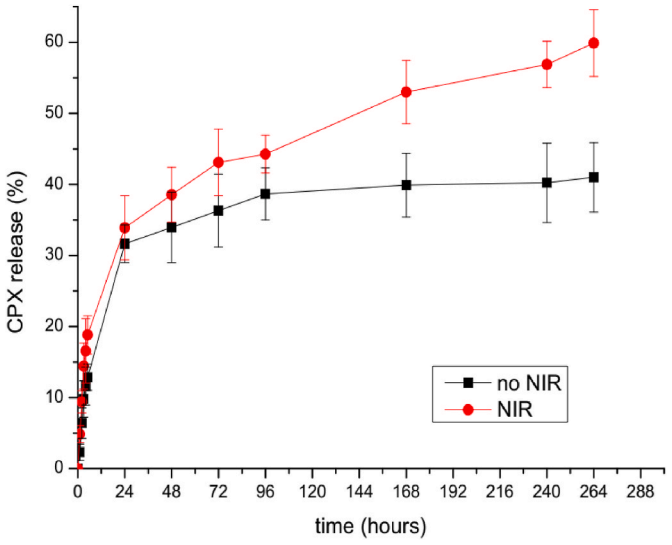

Fig. 10. NIR-triggered drug release from $PCI_{20\text{-}10}$ scaffold: Ciprofloxacin (CPX) release profiles from PCI_{20-10} in the presence and absence of NIR irradiation are reported over time. An initial burst release is observed within the first 24 h, followed by a sustained release phase. NIR irradiation significantly enhances CPX release, reaching ~60% compared to ~41% in non-irradiated conditions at the final time point. Data are expressed as mean ± SD, n = 3. The increased release under NIR is attributed to the photothermal effect induced by iron oxide nanoparticles, which likely promotes polymer chain mobility and accelerates drug diffusion. This behavior highlights the potential of $PCI_{20\text{-}10}$ scaffolds as on-demand drug delivery systems for localized therapy.

and roughly 60% of the drug remains unreleased over this timeframe. This behavior aligns with previous findings from our work on PBS-CPX patches [55]. Moreover, the release profile of $PCI_{20\text{-}10}$ appears comparable, suggesting that the iron-based nanoparticles within the patch do not play a significant role in CPX release.

$PCI_{20\text{-}10}$ was then subjected to a similar test with the addition of NIR irradiation. Specifically, the patch was irradiated to gain 40 °C followed by intermittent irradiation for 5 days as described in experimental setup. The results indicate that NIR exposure accelerates drug release and appears to promote a greater total release of CPX. After 11 days, about 60% of the loaded drug was released still without reaching a plateau. Based on these findings, the release behavior of PCI20-10 can be interpreted as a biphasic mechanism. In the absence of NIR irradiation, drug release is predominantly governed by diffusion from the polymer matrix, as evidenced by the gradual and incomplete release (~40% over 11 days), followed by a plateau. This behavior suggests diffusion-controlled transport driven by concentration gradients within the polymeric network. The observed plateau further indicates that a significant fraction of CPX remains physically entrapped within the fibers and becomes available only upon matrix relaxation or degradation. Upon NIR irradiation, a distinct release profile is observed, characterized by an increased release rate and higher cumulative release (~60% over 11 days, without reaching a plateau), indicating the contribution of a thermally enhanced mechanism. The localized heating induced by INP under NIR exposure is expected to increase polymer chain mobility and free volume, thereby facilitating drug diffusion. In addition, partial polymer relaxation or erosion may occur, contributing to non-Fickian transport behavior. Overall, while passive release is primarily diffusion-controlled, NIR irradiation introduces an additional thermally activated contribution that enhances both diffusion and matrix relaxation processes, resulting in a combined diffusion–relaxation mechanism. This interpretation is consistent with release behaviors commonly described in the literature for electrospun polymeric fibers systems, without requiring formal kinetic modeling [76]. This interpretation is further supported by the concentration-dependent behavior observed for $PCI_{5\text{-}10}$, where the absence of significant drug entrapment leads to rapid (5h) and complete release dominated by diffusion, without evidence of a secondary release phase. These findings further support the potential of the system as a controllable and externally responsive drug delivery platform.

3.6. Magnetic properties exploration

This section is devoted to investigating the magnetic behavior of the electrospun nanocomposite strip. To exploit its properties and analyze the hysteretic behavior in detail, particularly with respect to both expected trends and the predicted nonlinear response, the measurements were carried out using the experimental setup presented in Section 2.2.16. Magnetic analysis was carried out using the two sensing solutions described, in particular the first approach relied on a Hall sensor–based setup, while the second employed a fluxgate magnetometer. This dual strategy was adopted to enable both a comparative evaluation and a thorough analysis of the material's response to external magnetic excitation. In the Hall sensor–based configuration, two sensors were positioned to simultaneously measure the externally applied magnetic field and the stray magnetic field induced by the material (Fig. S5a of Supplementary materials). This arrangement enabled a direct comparison between the applied field and the resulting magnetic response of the sample, thereby providing an initial assessment of its superparamagnetic characteristics. To further investigate the material's response in greater detail, a second magnetometric setup was implemented using a fluxgate magnetometer (Figs. S5b and S8 of Supplementary Materials).

For the Hall sensor measurements, each experimental run was repeated ten times under the same operating conditions to allow for an assessment of signal variability. Repeated measurements were performed to account for fluctuations in the signals due to interference, external influences, and system-induced noise. The voltage outputs from both sensors were converted into magnetic field values using the calibration relationships presented in Equations (7) and (8). From these datasets, the mean, standard deviation, and corresponding error bars were calculated at each magnet–sample distance step. The resulting plot (Fig. 11) displays the applied magnetic field versus the stray field generated by the material, with error bars indicating the variability of the measurements.

This result shows, considering the variability range due to repeated measurements, that in the range of 197.5–200 mT, the response of the magnetic sensor due to the material's contribution does not exhibit a significant difference when the applied magnetic field is increased or decreased. Therefore, no hysteresis loop is observed; instead, within the measurement uncertainties, the two trends overlap.

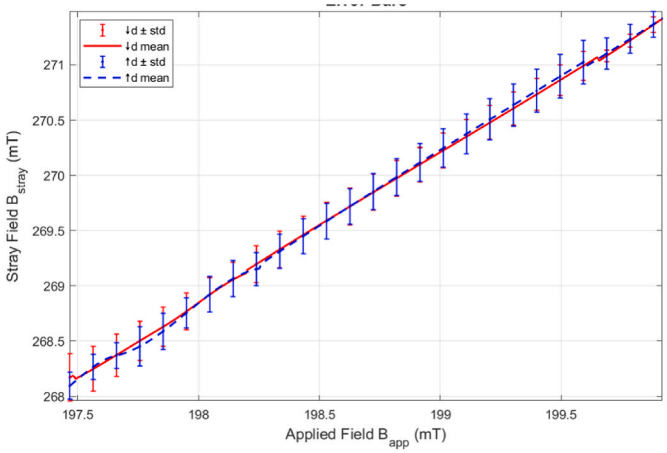

Fig. 11. Stray field as a function of applied field, showing mean values and error bars for increasing and decreasing magnet–sample distances.

For the fluxgate measurements, RTD of the output signal was processed following the same distance sweep protocol as used in the Hall sensor setup. At each magnet–sample separation, 1000 counts (with each count corresponding to an acquisition interval of 0.1 s) were recorded and averaged to obtain the mean RTD value, while standard deviations were calculated to evaluate measurement fluctuation and variability. The results were plotted as mean RTD versus magnet distance for both decreasing and increasing sweeps. Additionally, the material was tested in both vertical (Fig. 12a) and horizontal orientations (Fig. 12b).

The resulting curves highlight that the material exhibits nonlinear behavior, as expected. The combined use of Hall sensors and a fluxgate magnetometer provided complementary insights into the magnetic behavior of the electrospun nanocomposite strip.

It is worth noting that in both studies, repeated measurements demonstrated consistent and reproducible results. Minor deviations observed between increasing and decreasing distance sweeps suggest a weak hysteretic response; however, the overall loop remained narrow, indicating that the material does not retain significant magnetization once the external field is removed. This behavior is consistent with superparamagnetic characteristics, where the absence of coercivity and remanent magnetization confirms a fully reversible magnetization process.

The fluxgate magnetometer results reinforced and extended these observations by providing higher sensitivity in the low-field region, enabling the investigation of nonlinear effects in the hysteresis cycle. The RTD curves captured subtle variations in the magnetic response that were not fully resolved by the Hall sensors. In particular, the clear dependence of RTD values on magnet–sample distance, along with the near-overlap of increasing and decreasing sweeps, further confirmed the superparamagnetic nature of the material. At larger distances (55 mm), the fluxgate data revealed very low mean RTD values with minimal differences between sweeps, consistent with negligible magnetic interactions. As the magnets approached the sample (down to 30 mm), the RTD values increased sharply, reflecting the material's enhanced magnetic alignment under stronger applied fields. The absence of significant separation between the increasing and decreasing curves highlights the lack of magnetic memory, a defining feature of superparamagnetism.

Orientation-dependent measurements provided additional insight. When the stacked square samples were tested in both vertical and horizontal orientations, the fluxgate results showed only minor differences, suggesting that the magnetic response of the electrospun nanocomposite strip is almost isotropic within the tested configurations.

This observation strengthens the reliability of the conclusions, indicating that the measured superparamagnetic behavior is an intrinsic property of the material rather than an artifact of sample alignment or geometry. It is worth noting that the Hall sensor setup proved valuable for establishing baseline trends and validating the applied–stray field relationship, while the fluxgate magnetometer delivered the performance necessary to resolve fine variations and confirm the absence of remanence and coercivity. Overall, these results confirm that the incorporation of INPs enables reliable superparamagnetic behavior, supporting the multifunctional and theranostic potential of the developed scaffolds.

3.7. Evaluation of the biocompatibility of the magnetic nano-electrospuns

To assess the potential use of the material for biomedical applications, we conducted in vitro biocompatibility studies using two cell lines: fibroblasts (HGF1) and keratinocytes (HaCaT). A detailed analysis of the results (see graphs in Fig. 13) showed that after 24 h, both HaCaT and HGF1 cells exhibited cell viability values above 90%. At 48 h, cell viability remained high, ranging from 86.5% (PCI20-10 with HGF1) to 91.5% (PCI5-10 with HaCaT). HaCaT cells consistently showed slightly higher viability than HGF1 cells. Data are presented as mean ± SD of technical triplicates and normalized to untreated control (100%). Statistical analysis was performed using one-way ANOVA followed by Holm–Šidák multiple comparisons test. No statistically significant differences were observed among groups ($p > 0.05$). Overall, the patches demonstrated excellent cytocompatibility at both times, supporting their suitability for biomedical applications. These biological outcomes can be correlated with key material properties. The hydrophilic surface of the scaffolds, as evidenced by wettability measurements, likely promoted favorable cell environment. Furthermore, surface exposure of ciprofloxacin may have contributed to the absence of cytotoxic effects, while the incorporation of iron nanoparticles, at both concentrations, did not negatively impact cell viability, consistent with the known biocompatibility of these superparamagnetic materials. Collectively, these observations suggest that the material's surface chemistry and composition synergistically support cellular compatibility. These results further confirm the suitability of the developed scaffolds for biomedical applications requiring both functional responsiveness and biocompatibility.

4. Conclusions

In this work, iron oxide nanopowder (INP) was successfully incorporated as a photo-thermal agent into electrospun fibers through a one-step optimized process. Poly(butylene succinate) (PBS)-based PCI scaffolds loaded with ciprofloxacin (CPX) and INP were fabricated, yielding

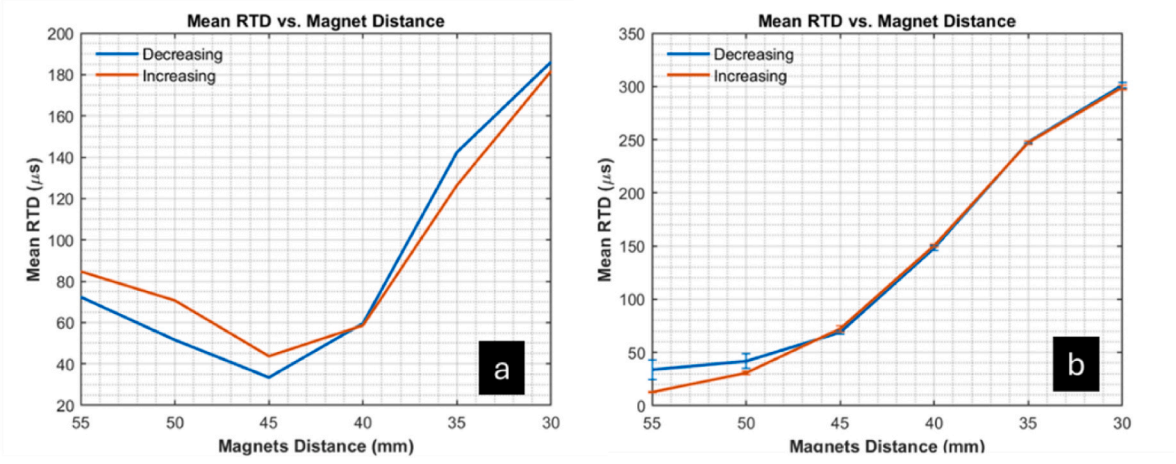

Fig. 12. (a) Mean RTD values as a function of magnet–sample distance for decreasing and increasing sweeps for the vertical orientation. (b) Mean RTD values as a function of magnet–sample distance for decreasing and increasing sweeps for the horizontal orientation.

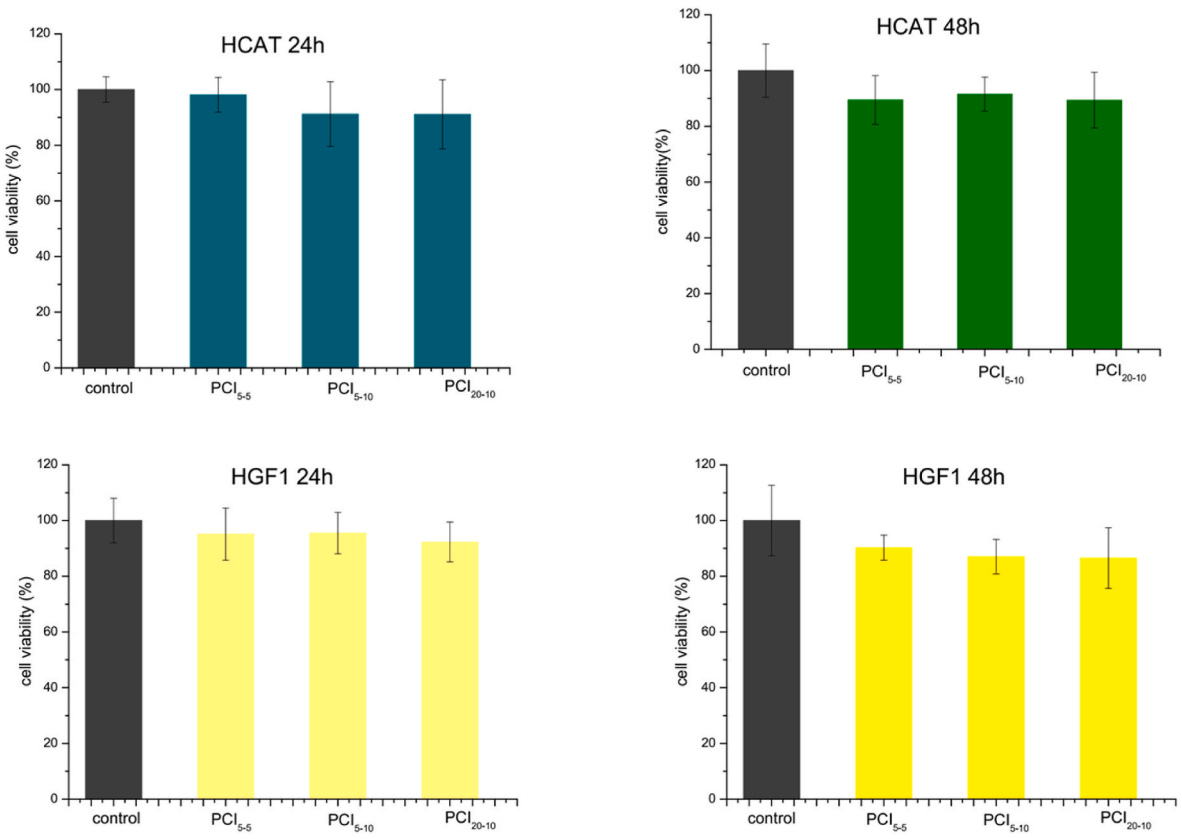

Fig. 13. Human gingival fibroblast (HGF1) and immortal keratinocyte from adult human skin (HaCaT) viability on PCI scaffolds after 24h and 48h incubation at 37 °C. Data are presented as mean ± SD of technical triplicates and normalized to untreated control (100%). Statistical analysis was performed using one-way ANOVA followed by Holm–Šidák multiple comparisons test. No statistically significant differences were detected among groups ($p > 0.05$); no significance indicators are shown.

uniform and defect-free fibers with homogeneous drug and nanoparticle distribution, high iron loading efficiency (up to 50%), and complete CPX encapsulation. The presence of CPX improved fiber morphology by increasing the electrical conductivity of the spinning solution and enhanced wettability and water uptake, effectively overcoming the intrinsic hydrophobicity of PBS and promoting a more biocompatible surface. The scaffolds exhibited suitable water vapor transmission rates, supporting their potential application in wound healing, while thermal and spectroscopic analyses confirmed the amorphous state of CPX and its uniform dispersion within the polymer matrix. Magnetic characterization demonstrated superparamagnetic behavior, while imaging analyses confirmed X-ray detectability and MRI visibility, enabling non-invasive monitoring. The absence of iron release over 30 days indicated strong nanoparticle retention and long-term stability. Upon NIR irradiation, the scaffolds exhibited a controllable photothermal response dependent on INP content, enabling modulation of drug release. A biphasic release profile governed by diffusion and matrix relaxation was observed, with NIR stimulation significantly enhancing both the rate and extent of CPX release, confirming the feasibility of externally triggered drug delivery. In vitro biocompatibility studies using fibroblasts (HGF1) and keratinocytes (HaCaT) showed high cell viability (>85%), confirming the non-cytotoxic nature of the scaffolds according to ISO 10993, with no statistically significant differences observed among experimental conditions ($p > 0.05$). Compared to conventional SPION-based systems, the use of dry iron oxide nanopowder enables a simpler, scalable, and cost-effective strategy while maintaining magnetic and photothermal functionalities. The integration of NIR-triggered drug release within electrospun scaffolds, still scarcely explored, further highlights the novelty of the proposed approach. Beyond wound healing, this platform shows potential for extension toward multifunctional biomedical devices, including drug-loaded tubular constructs for vascular graft applications, with the additional advantage of MRI-based monitoring. Preliminary observations also suggest sensitivity to mechanical deformation through variations in magnetic response, which will be further investigated. Overall, PCI scaffolds represent a scalable and cost-effective multifunctional platform integrating controlled drug delivery, photo-thermal responsiveness, magnetic detectability, and imaging capability. By combining therapeutic and diagnostic functionalities, this system shows strong potential as a theranostic biomaterial for advanced biomedical applications, including localized antibacterial therapy, tissue regeneration, and anticancer treatment, paving the way toward more effective and personalized therapeutic strategies.

Statement: During the preparation of this work the authors used ChatGPT, OpenAI exclusively for language editing and improvement purposes, such as grammar, style, and clarity enhancement. No part of the data analysis, experimental design, interpretation of results, or generation of scientific content was performed by AI. After using this tool, the authors reviewed and edited the content as needed and take full responsibility for the content of the published article.

CRediT authorship contribution statement

Sergio Sciré: Conceptualization, Data curation, Formal analysis, Investigation, Methodology, Writing – original draft, Writing – review & editing. **Achraf Derbel:** Data curation, Formal analysis, Investigation, Methodology. **Francesca Terracina:** Data curation, Formal analysis, Investigation, Methodology. **Emanuela Fabiola Craparo:** Data curation, Formal analysis, Investigation, Methodology. **Luca Cicero:** Data curation, Formal analysis, Investigation, Methodology. **Giovanni Cassata:** Data curation, Formal analysis, Investigation, Methodology,

Supervision. **Carlo Trigona:** Data curation, Investigation, Methodology, Writing – original draft, Writing – review & editing. **Mariano Licciardi:** Conceptualization, Data curation, Investigation, Resources, Supervision, Validation, Writing – original draft, Writing – review & editing.

Declaration of competing interest

The authors declare that they have no known competing financial interests or personal relationships that could have appeared to influence the work reported in this paper.

Acknowledgements

The authors thanks SiciliAn MicronanOTecH Research And Innovation CEnter "SAMOTHRACE" (MUR, PNRR-M4C2, ECS_00000022), spoke 3 - Universita 'degli Studi di Palermo S2-COMMs - Micro and Nanotechnologies for Smart & Sustainable Communities, for funding.

The authors thank the Advanced Technologies Network Center (ATeN Center) of the University of Palermo, Laboratory of Preparation and Analysis of Biomaterials, for the contact angle measurements, scansion electron microscopy micrographs, Micro CT and electrospinning facility access.

The author thanks the Istituto Zooprofilattico della Lombardia for providing the cells HaCaT and HGF-1 at a special price for non-profit research institutions.

Appendix A. Supplementary data

Supplementary data to this article can be found online at https://doi.org/10.1016/j.jddst.2026.108250.

Data availability

Data will be made available on request.

References

[1] F.Y. Dong Liu, The smart drug delivery system and its clinical potential, Theranostics 6 (9) (2016) 1306–1323, https://doi.org/10.7150/thno.14858.
[2] Z. Chen, S. Song, Fabrication of magnetic core/shell hydrogels via microfluidics for controlled drug delivery, Chem. Eng. Sci. (2022), https://doi.org/10.1016/j.ces.2021.117216.
[3] S. Kanwar, S. Vijayavenkataraman, 3D-printed polycaprolactone-magnetic nanoparticles composite multifunctional scaffolds for bone tissue regeneration and hyperthermia treatment, Int. J. Bioprint. 10 (6) (2024) 4538, https://doi.org/10.36922/ijb.4538.
[4] Z.Q. Zhang, S.C. Song, Multiple hyperthermia-mediated release of TRAIL/SPION nanocomplex from thermosensitive polymeric hydrogels for combination cancer therapy, Biomaterials (2017), https://doi.org/10.1016/j.biomaterials.2017.03.049.
[5] A. Raza, U. Hayat, T. Rasheed, M. Bilal, H.M.N. Iqbal, "Smart" materials-based near-infrared light-responsive drug delivery systems for cancer treatment: a review, J. Mater. Res. Technol. 8 (2019) 1497–1509, https://doi.org/10.1016/j.jmrt.2018.03.007.
[6] Y. He, J. Leng, K. Li, K. Xu, C. Lin, Z. Yuan, R. Zhang, D. Wang, B. Tao, T.J. Huang, K. Cai, A multifunctional hydrogel coating to direct fibroblast activation and infected wound healing via simultaneously controllable photobiomodulation and photodynamic therapies, Biomaterials (2021), https://doi.org/10.1016/j.biomaterials.2021.121164.
[7] X. Yin, T. Fan, Palladium nanoparticle based smart hydrogels for NIR light-triggered photothermal/photodynamic therapy and drug release with wound healing capability, Nanoscale Adv. 5 (2023) 1729–1739, https://doi.org/10.1039/d2na00897a.
[8] E. Hemmer, A. Benayas, Exploiting the biological windows: current perspectives on fluorescent bioprobes emitting above 1000 nm, Nanoscale Horiz. (2016).
[9] G. Strangman, J.P. Culver, J.H. Thompson, D.A. Boas, A quantitative comparison of simultaneous BOLD fMRI and NIRS recordings during functional brain activation, Neuroimage 17 (2) (2002) 719–731.
[10] M. Dehghankhold, F. Ahmadi, N. Nezafat, M. Abedi, P. Iranpour, A. Dehghanian, O. Koohi-Hosseinabadi, A.R. Akbarizadeh, Z. Sobhani, A versatile theranostic magnetic polydopamine iron oxide NIR laser-responsive nanosystem containing doxorubicin for chemo-photothermal therapy of melanoma, Biomater. Adv. (2024), https://doi.org/10.1016/j.bioadv.2024.213797.
[11] Y. Wang, Y. Xu, J. Song, X. Liu, S. Liu, N. Yang, L. Wang, Y. Liu, Y. Zhao, W. Zhou, Y. Zhang, Tumor cell-targeting and tumor microenvironment-responsive nanoplatforms for the multimodal imaging-guided photodynamic/photothermal/chemodynamic treatment of cervical cancer, Int. J. Nanomed. 19 (2024 Jun 13) 5837–5858, https://doi.org/10.2147/IJN.S466042. PMID: 38887692; PMCID: PMC11182360.
[12] L. Huang, Y. Luo, Y. Cong, J. Liu, C. Xu, Z. Zeng, Y. Yin, H. Hong, W. Xu, Metal–organic framework-based pH/NIR dual-responsive nanoparticles for combined photothermal/photodynamic therapy and chemotherapy of cancer, New J. Chem. 19 (2024), https://doi.org/10.1039/D3NJ04916G.
[13] R.P. Gambhir, A.A. Vibhute, T.P. Patil, A.P. Tiwari, Surface-functionalized iron oxide (Fe_3O_4) nanoparticles for biomedical applications, in: F.I. Ezema, C. D. Lokhande, A.C. Lokhande (Eds.), Chemically Deposited Metal Chalcogenide-based Carbon Composites for Versatile Applications, Springer, Cham, 2023, https://doi.org/10.1007/978-3-031-23401-9_15.
[14] X. Chen, X. Ren, Y. Wang, J. Meng, Q. Huang, J. Shen, Construction of a multifunctional janus nanofiber membrane based on tannic acid-Fe complexes for photothermal/drug synergistic antibacteria, ACS Appl. Polym. Mater. 6 (2024) 15345–15354.
[15] R. Cillari, S. Scirè, G. Cavallaro, N. Mauro, in: Ultrasmall Glucose-Functionalized Au-Carbon Nanohybrids: Exploiting the Warburg Effect to Image Tumors by Multimodal CT/Fluorescence Imaging, 10, 2024, p. 35, https://doi.org/10.3390/c10020035.
[16] A. Holca, R. Borlan, A. Campu, S. Dragan, M. Muntean, A.-M. Craciun, A. Sesarman, M. Banciu, S. Astilean, M. Lamy de la Chapelle, M. Focsan, LED-activated NIR-II gold nanorods for photothermal therapy of 3D melanoma spheroids, ACS Appl. Nano Mater. 8 (41) (2025) 19796–19809, https://doi.org/10.1021/acsanm.5c03202.
[17] M. Licciardi, P. Varvarà, L. Tranchina, R. Puleio, L. Cicero, G. Cassata, G. Giammona, In vivo efficacy of verteporfin loaded gold nanorods for combined photothermal/photodynamic colon cancer therapy, Int. J. Pharm. 625 (2022) 122134, https://doi.org/10.1016/j.ijpharm.2022.122134.
[18] R. Puleio, M. Licciardi, P. Varvarà, C. Scialabba, G. Cassata, L. Cicero, G. Cavallaro, G. Giammona, Effect of actively targeted copolymer coating on solid tumors eradication by gold nanorods-induced hyperthermia, Int. J. Pharm. 587 (2020) 119641, https://doi.org/10.1016/j.ijpharm.2020.119641.
[19] R. Zhang, J. Shi, Z. Song, et al., A synergistically enhanced photothermal transition effect from mesoporous silica nanoparticles with gold nanorods wrapped in reduced graphene oxide, J. Mater. Sci. 53 (3) (2018) 1810–1823, https://doi.org/10.1007/s10853-017-1628-y.
[20] C. Shuai, Z. Yu, F. Qi, T. He, D. Zhang, X. Shuai, M. Yang, NIR-plasmon enhanced MXene/Fe-MOFs composite scaffold for synergistic chemodynamic-photothermal antibacterial therapy in bone implants, ACS Appl. Bio Mater. 8 (8) (2025) 7331–7343, https://doi.org/10.1021/acsabm.5c01000.
[21] H. Guo, Y. Liu, C. Fang, X. Yan, K. Zhang, H. Gao, The cutting-edge progress in covalent organic framework-based nanomedicine, Adv. NanoBiomed Res. 4 (2024) 2300163, https://doi.org/10.1002/anbr.202300163.
[22] M. Zhao, J. Huang, H. Yang, R. Yang, S. Guo, Z. Liu, Q. Xie, M. Li, Z. Fan, P. Xiao, Z. Zhang, X. Chen, X. Li, Q. Zeng, B. Li, Y. Wu, M. Kang, J. Zheng, D. Wang, Y. Liao, Engineered aggregation-induced emission luminogens-based framework with CO-releasing property for accelerating diabetic wound healing, Chem. Eng. J. (2025), https://doi.org/10.1016/j.cej.2025.168981.
[23] Q. Cui, K. Zhang, X. Fei, C. Wang, S. Cheng, Y. Li, L. Xu, Thermoresponsive hydrogel dressings for precision drug release under physiological conditions, Eur. Polym. J. 237 (2025), https://doi.org/10.1016/j.eurpolymj.2025.09.017.
[24] A. Nicosia, G. Cavallaro, S. Costa, M.A. Utzeri, A. Cuttitta, G. Giammona, N. Mauro, Carbon nanodots for on demand chemophotothermal therapy combination to elicit necroptosis: overcoming apoptosis resistance in breast cancer cell lines, Cancers 12 (11) (2020) 3114, https://doi.org/10.3390/cancers12113114.
[25] P. Varvarà, N. Mauro, G. Cavallaro, Targeted NIR-triggered doxorubicin release using carbon dots–poly(ethylene glycol)–folate conjugates for breast cancer treatment, Nanoscale Adv. 7 (2025) 862–875, https://doi.org/10.1039/D4NA00834K.
[26] M. Overchuk, R.A. Weersink, B.C. Wilson, G. Zheng, Photodynamic and photothermal therapies: synergy opportunities for nanomedicine, ACS Nano 17 (2023) 7979–8003.
[27] S. Sciré, M. Bianchi, M. Pensabene, A. Dorigato, N. Mauro, A robust, biocompatible scaffold for peripheral nerve regeneration: integration of PLLA nanofibers with a RGD-like poly(amidoamine) hydrogel, Eur. Polym. J. 235 (2025) 114097, https://doi.org/10.1016/j.eurpolymj.2025.114097.
[28] H.A. Abboud, R. Zelkó, A. Kazsoki, A systematic review of liposomal nanofibrous scaffolds as a drug delivery system: a decade of progress in controlled release and therapeutic efficacy, Drug Deliv. 32 (1) (2024), https://doi.org/10.1080/10717544.2024.2445259.
[29] Y. Yuan, L.C. Madruga, K.Y. Cotton, M.J. Kipper, S.R. Khetani, Biochemical and biophysical properties of extracellular matrix nanofibers modulate iPSC-derived human hepatocyte maturation, J. Biomed. Mater. Res. 113 (10) (2025) e37998, https://doi.org/10.1002/jbm.a.37998.
[30] J. Liu, K. Wang, F. Jin, Y. Bin, J. Li, X. Qian, Advances in photothermal electrospinning: from fiber fabrication to biomedical application, Polymers 17 (13) (2025) 1725, https://doi.org/10.3390/polym17131725.
[31] R.R. Qiao, C. Yu, Superparamagnetic iron oxide nanoparticles: from preparations to in vivo MRI applications, J. Mater. Chem. 19 (35) (2009) 6274–6293.
[32] L. Affatigato, M. Licciardi, M.C. D'Oca, L. Cicero, A. Bonamore, A. Incocciati, A. Macone, C.D. Buch, S. Piligkos, A. Boffi, V. Militello, Ferritin coated SPIONs as new cancer cell targeted magnetic nanocarrier, Molecules 28 (2023) 1163, https://doi.org/10.3390/molecules28031163.

[33] L. Affatigato, M. Licciardi, M.C. D'Oca, L. Cicero, A. Bonamore, A. Incocciati, A. Macone, C.D. Buch, S. Piligkos, A. Boffi, V. Militello, Magnetic and MRI contrast properties of HumAfFt-SPIONs: investigating superparamagnetic behavior and enhanced T2-weighted imaging performance, Int. J. Mol. Sci. 26 (2025) 3505, https://doi.org/10.3390/ijms26083505.
[34] M. Licciardi, C. Scialabba, R. Puleio, G. Cassata, L. Cicero, G. Cavallaro, G. Giammona, Smart copolymer coated SPIONs for colon cancer chemotherapy, Int. J. Pharm. 556 (2019) 57–67, https://doi.org/10.1016/j.ijpharm.2018.11.069.
[35] N. Mauro, C. Scialabba, R. Puleio, P. Varvarà, M. Licciardi, G. Cavallaro, G. Giammona, SPIONs embedded in polyamino acid nanogels to synergistically treat tumor microenvironment and breast cancer cells, Int. J. Pharm. 555 (2019) 207–219, https://doi.org/10.1016/j.ijpharm.2018.11.046.
[36] C. Öziç, E. Ertaş, M.F. Baran, A. Baran, E. Ahmadian, A. Eftekhari, R. Khalilov, E. Aliyev, M. Yıldıztekin, Synthesis and characterization of activated carbon-supported magnetic nanocomposite (MNPs-OLAC) obtained from okra leaves as a nanocarrier for targeted delivery of morin hydrate, Front. Pharmacol. 15 (2024) 1482130, https://doi.org/10.3389/fphar.2024.1482130.
[37] M. Bonini, D. Berti, Nanostructures for magnetically triggered release of drugs and biomolecules, Curr. Opin. Colloid Interface Sci. 18 (5) (2013) 459–467.
[38] H. Markides, M. Rotherham, A.J. El Haj, Biocompatibility and toxicity of magnetic nanoparticles in regenerative medicine, Nanomaterials (2012), https://doi.org/10.1155/2012/614094.
[39] A. Van de Walle, J. Kolosnjaj-Tabi, Y. Lalatonne, C. Wilhelm, Ever-evolving identity of magnetic nanoparticles within human cells: the interplay of endosomal confinement, degradation, storage, and neocrystallization, Acc. Chem. Res. 53 (10) (2020) 2212–2224, https://doi.org/10.1021/acs.accounts.0c00355.
[40] M. Chu, Y. Shao, Near-infrared laser light mediated cancer therapy by photothermal effect of Fe3O4 magnetic nanoparticles, Biomaterials 34 (16) (2013) 4078–4088, https://doi.org/10.1016/j.biomaterials.2013.01.086.
[41] E.A. Périgo, G. Hemery, O. Sandre, D. Ortega, E. Garaio, F. Plazaola, F.J. Teran, Fundamentals and advances in magnetic hyperthermia, Appl. Phys. Rev. 2 (4) (2015) 041302, https://doi.org/10.1063/1.4935688.
[42] A. Espinosa, R. Di Corato, J. Kolosnjaj-Tabi, P. Flaud, T. Pellegrino, C. Wilhelm, Duality of iron oxide nanoparticles in cancer therapy: amplification of heating efficiency by magnetic hyperthermia and photothermal bimodal treatment, ACS Nano 10 (2) (2016) 2436–2446, https://doi.org/10.1021/acsnano.5b07249.
[43] C. Lozano-Pedraza, E. Plaza-Mayoral, A. Espinosa, B. Sot, A. Serrano, G. Salas, C. Blanco-Andujar, G. Cotin, D. Felder-Flesch, S. Begin-Colin, F.J. Teran, Assessing the parameters modulating optical losses of iron oxide nanoparticles under near infrared irradiation, Nanoscale Adv. 3 (2021) 6490–6502, https://doi.org/10.1039/d1na00601k.
[44] F. Ozel, H. Kockar, S. Beyaz, et al., Superparamagnetic iron oxide nanoparticles: effect of iron oleate precursors obtained with a simple way, J. Mater. Sci. Mater. Electron. (2013), https://doi.org/10.1007/S10854-013-1213-3.
[45] M. Gigli, M. Fabbri, N. Lotti, R. Gamberini, B. Rimini, A. Munari, Poly(butylene succinate)-based polyesters for biomedical applications: a review, Eur. Polym. J. 75 (2016) 431–460, https://doi.org/10.1016/j.eurpolymj.2016.01.016.
[46] M. Barletta, C. Aversa, M. Ayyoob, A. Gisario, K. Hamad, M. Mehrpouya, H. Vahabi, Poly(butylene succinate) (PBS): materials, processing, and industrial applications, Prog. Polym. Sci. 132 (2022) 101579, https://doi.org/10.1016/j.progpolymsci.2022.101579.
[47] G.E. Vigni, M. Licciardi, L. D'itri, F. Terracina, S. Scirè, G. Arrabito, B. Pignataro, L. Camarda, G. Cassata, R. Puleio, et al., Improved bone regeneration using biodegradable polybutylene succinate artificial scaffold with BMP-2 protein in a rabbit model, Materials 18 (2025) 2234, https://doi.org/10.3390/ma18102234.
[48] G. Di Prima, M. Licciardi, F. Carfì Pavia, A.I. Lo Monte, G. Cavallaro, G. Giammona, Microfibrillar polymeric ocular inserts for triamcinolone acetonide delivery, Int. J. Pharm. 567 (2019 Aug 15) 118459, https://doi.org/10.1016/j.ijpharm.2019.118459. Epub 2019 Jun 24. PMID: 31247275.
[49] L. Cicero, M. Licciardi, R. Cirincione, R. Puleio, G. Giammona, G. Giglia, P. Sardo, G. Vigni, A. Cioffi, A. Sanfilippo, G. Cassata, Polybutylene succinate artificial scaffold for peripheral nerve regeneration, J. Biomed. Mater. Res. B Appl. Biomater. 110 (2022) 125–134, https://doi.org/10.1002/jbm.b.34896.
[50] G.C. Miceli, F.S. Palumbo, F.P. Bonomo, M. Zingales, M. Licciardi, Polybutylene succinate processing and evaluation as a micro fibrous graft for tissue engineering applications, Polymers 14 (21) (2022) 4486, https://doi.org/10.3390/polym14214486.
[51] G.E. Vigni, G. Cassata, G. Caldarella, R. Cirincione, M. Licciardi, G.C. Miceli, R. Puleio, L. D'Itri, R. Lo Coco, L. Camarda, L. Cicero, Improved bone regeneration using biodegradable polybutylene succinate artificial scaffold in a rabbit model, J. Funct. Biomater. 14 (2023) 22, https://doi.org/10.3390/jfb14010022.
[52] L. Cicero, G. Puleio, R. Cassata, R. Cirincione, L. Camarda, D. Caracappa, L. D'Itri, M. Licciardi, G.E. Vigni, Peripheral nerve regeneration at 1 year: biodegradable polybutylene succinate artificial scaffold vs. conventional epineurial sutures, Polymers 15 (2023) 3398, https://doi.org/10.3390/polym15163398.
[53] G. Puleo, F. Terracina, V. Catania, S. Scirè, D. Schillaci, M. Licciardi, Electrosprayed poly-butyl-succinate microparticles for sustained release of Ciprofloxacin as an antimicrobial delivery system, Powder Technol. 432 (2024) 119152, https://doi.org/10.1016/j.powtec.2023.119152.
[54] C. Scolaro, S. Brahimi, A. Falcone, V. Beghetto, A. Visco, Mechanical and physical changes in bio-polybutylene-succinate induced by UVC ray photodegradation, Polymers 16 (9) (2024) 1288, https://doi.org/10.3390/polym16091288.
[55] F. Terracina, S. Scirè, G. Puleo, V. Catania, A.I. Lo Monte, D. Schillaci, M. Licciardi, Polybutylene succinate-based electrospun scaffolds improving skin permeation of the antibacterial ciprofloxacin, J. Drug Deliv. Sci. Technol. 107 (2025) 106815, https://doi.org/10.1016/j.jddst.2025.106815.
[56] Y. Pan, S. Neuss, A. Leifert, M. Fischler, F. Wen, U. Simon, G. Schmid, W. Brandau, W. Jahnen-Dechent, Size-dependent cytotoxicity of gold nanoparticles, Small 3 (2007) 1941–1949.
[57] C. Trigona, S. Graziani, S. Baglio, Changes in sensors technologies during the last ten years: evolution or revolution? IEEE Instrum. Meas. Mag. 23 (6) (2020) 18–22.
[58] P. Ripka, Magnetic Sensors and Magnetometers, Artech House, 2021.
[59] J.F.D.F. Araujo, J.M.B. Pereira, A.C. Bruno, Assembling a magnetometer for measuring the magnetic properties of iron oxide microparticles in the classroom laboratory, Am. J. Phys. 87 (6) (2019), https://doi.org/10.1119/1.5100944.
[60] C. Trigona, V. Sinatra, B. Andò, S. Baglio, A.R. Bulsara, Flexible microwire residence times difference fluxgate magnetometer, IEEE Trans. Instrum. Meas. 66 (3) (2017) 559–568.
[61] N.S. Kommareddi, M. Tata, V.T. John, G.L. McPherson, M.F. Herman, Y.-S. Lee, C. J. O'Connor, J.A. Akkara, D.L. Kaplan, Synthesis of superparamagnetic polymer–ferrite composites using surfactant microstructures, Chem. Mater. 8 (3) (1996) 801–809, https://doi.org/10.1021/cm940485o.
[62] C. Trigona, B. Andò, V. Sinatra, C. Vacirca, E. Rossino, L. Palermo, S. Baglio, Implementation and characterization of a smart parking system based on 3-axis magnetic sensors, in: 2016 IEEE International Instrumentation and Measurement Technology Conference Proceedings, IEEE, 2016, pp. 1–6.
[63] S. Yenuganti, S.S. Raju, H. Settibhaktini, A brief review of Hall effect-based sensors, Sens. Rev. (2025) 1–23.
[64] F. Kaluza, A. Grüger, H. Grüger, New and future applications of fluxgate sensors, Sensor Actuator Phys. 106 (1-3) (2003) 48–51.
[65] C. Trigona, V. Sinatra, B. Andò, S. Baglio, A.R. Bulsara, G. Mostile, M. Zappia, Measurements of iron compound content in the brain using a flexible core fluxgate magnetometer at room temperature, IEEE Trans. Instrum. Meas. 67 (4) (2018) 971–980.
[66] J.G. Hodge, D.S. Zamierowski, J.L. Robinson, A.J. Mellott, Evaluating polymeric biomaterials to improve next generation wound dressing design, Biomater. Res. 26 (1) (2022) 50, https://doi.org/10.1186/s40824-022-00291-5.
[67] I. Turel, I. Leban, N. Bukovec, Crystal structure and characterization of the bismuth (III) compound with quinolone family member (ciprofloxacin): antibacterial study, J. Inorg. Biochem. 66 (4) (1997) 241–245, https://doi.org/10.1016/S0162-0134(96)00218-8.
[68] I. Turel, P. Bukovec, M. Quirós, Crystal structure of ciprofloxacin hexahydrate and its characterization, Int. J. Pharm. 152 (1) (1997) 59–65, https://doi.org/10.1016/S0378-5173(97)04913-2.
[69] F. Gao, P. Yang, J. Xie, H. Wang, Synthesis, characterization and antibacterial activity of novel Fe(III), Co(II), and Zn(II) complexes with norfloxacin, J. Inorg. Biochem. 60 (1) (1995) 61–67, https://doi.org/10.1016/0162-0134(95)00002-6.
[70] V. Ghaffarian, S.M. Mousavi, M. Bahreini, H. Jalaei, Polyethersulfone/poly (butylene succinate) membrane: effect of preparation conditions on properties and performance, J. Ind. Eng. Chem. 20 (4) (2014) 1359–1366, https://doi.org/10.1016/j.jiec.2013.07.019.
[71] A.S. Figueiredo, L.P. Icart, F.D. Marques, E.R. Fernandes, L.P. Ferreira, G. E. Oliveira, F.G. Souza Jr., Extrinsically magnetic poly(butylene succinate): an up-and-coming petroleum cleanup tool, Sci. Total Environ. 647 (2019) 88–98, https://doi.org/10.1016/j.scitotenv.2018.07.421.
[72] X. Wang, J. Zhou, L. Li, Multiple melting behavior of poly(butylene succinate), Eur. Polym. J. 43 (8) (Aug. 2007) 3163–3170, https://doi.org/10.1016/j.
[73] A.A. Silva-Júnior, M.V. Scarpa, K.C. Pestana, L.P. Mercuri, J.R. de Matos, A.G. de Oliveira, Thermal analysis of biodegradable microparticles containing ciprofloxacin hydrochloride obtained by spray drying technique, Thermochim. Acta 467 (1–2) (2007) 91–98, https://doi.org/10.1016/j.tca.2007.10.018.
[74] J. Liu, H. Zheng, P.S.P. Poh, H.-G. Machens, A.F. Schilling, Hydrogels for engineering of perfusable vascular networks, Int. J. Mol. Sci. 16 (2015) 15997–16016, https://doi.org/10.3390/ijms160715997.
[75] J. Fu, D. Wang, Z. Tang, Y. Xu, J. Xie, R. Chen, P. Wang, Q. Zhong, Y. Ning, M. Lei, H. Mai, H. Li, H. Liu, J. Wang, H. Cheng, NIR-responsive electrospun nanofiber dressing promotes diabetic-infected wound healing with programmed combined temperature-coordinated photothermal therapy, J. Nanobiotechnol. 22 (1) (2024 Jul 1) 384, https://doi.org/10.1186/s12951-024-02621-2. PMID: 38951903; PMCID: PMC11218286.
[76] J. Sthuthi, S. Shanmugam, A review of electrospun polymeric fibers as potential drug delivery systems for tunable release kinetics, J. Sci. Adv. Mater. Devices 10 (3) (2025) 100933, https://doi.org/10.1016/j.jsamd.2025.100933.